Novel dopaminergic neurotransmission in the *Octopus* visual system

Amy Courtney[1], Ruth Styfhals[2], Marie Van Dijck[2], Jérôme Boulanger[1], Lieve Geenen[2], Maxence Lanoizelet[2], Iris Hardege[3], Mark Lassnig[2], Anna M. Jansson[1], Joseph Gehler-Rahman[1], Eduardo Almansa[4], Horst A. Obenhaus[5], Eve Seuntjens[2]§, William R. Schafer[1,2]§*.

1. MRC Laboratory of Molecular Biology, Cambridge, UK.
2. Department of Biology, KU Leuven, Leuven, Belgium.
3. Department of Zoology, University of Cambridge, UK.
4. Oceanographic Centre of Canary Islands, Spanish Institute of Oceanography, CSIC, Tenerife, Spain.
5. Kavli Institute for Systems Neuroscience and Centre for Neural Computation, Norwegian University of Science and Technology, Trondheim, Norway.

§ Senior authors (equal contribution)

* Corresponding Author

Summary

Coleoid cephalopods such as the common octopus have a complex visual system, with a camera-type eye and a large optic lobe, that evolved independently from its counterpart in vertebrates. However, the molecular and neurochemical basis of signalling in *Octopus* visual circuits is not well understood. Through heterologous expression of ligand-gated ion channel genes from *Octopus vulgaris,* we have identified and characterised novel ionotropic receptors for two of the major optic lobe neurotransmitters, dopamine and acetylcholine. One of these, DopC1, defines a new class of dopamine-gated cation channels that is broadly conserved in many invertebrates. Dopamine robustly stimulates neural activity in the optic lobe, particularly in layers where DopC1 is expressed, consistent with a role for this channel in excitatory neurotransmission. A second protein, AChRB1, forms acetylcholine-gated anion channels and is implicated in inhibition of dopaminergic amacrine cells in the outer granular layer (OGL). This combination of inhibitory cholinergic input and excitatory dopaminergic output may allow OGL amacrine cells to carry out lateral inhibition; thus, despite their very different functional and neurochemical properties, *Octopus* amacrine cells may execute similar computations to amacrine and horizontal cells in the vertebrate retina.

36 # Introduction

37 Coleoid cephalopods, such as squid, cuttlefish and octopus, are notable for their large brains
38 and complex behaviour. For example, the nervous system of the common octopus, *Octopus*
39 *vulgaris*, contains approximately 500 million neurons[1], more than some mammals[2], and
40 supports intricate behaviours such as camouflage, tool use, visually-guided hunting, and
41 sophisticated learning and memory[3]. However, octopuses and humans diverged evolutionarily
42 approximately 600 million years ago, early in the bilaterian lineage, from a common ancestor
43 with a much simpler nervous system[4]. Thus, the complex brains of cephalopods appear to
44 have evolved independently from those of vertebrates. Gaining a better understanding of
45 cephalopod neural circuits will therefore shed light on the general principles that underpin
46 complex behaviour across species, as well as discover new biology and species-specific
47 innovations.

48 The visual system represents a particularly relevant opportunity to compare cephalopod and
49 vertebrate neural circuitry. Vision is an important sensory modality for cephalopods, driving
50 complex visually guided behaviours including camouflage, hunting, mating and learning[5].
51 Like vertebrates, cephalopods have a camera-type eye that projects visual scenes onto a retina
52 consisting of a single layer of photoreceptors , which direct their output to the cortex of the
53 optic lobe (OL), comprised of three layers: an outer (OGL) and inner (IGL) granular layer
54 containing neuronal cell bodies separated by a plexiform layer composed only of neuropil,
55 including the end terminals of photoreceptors[6]. The OGL consists exclusively of neurons with
56 amacrine morphology, which extend processes within the plexiform layer. The IGL contains
57 a diverse population of neurons, including another population of amacrine cells that arborize
58 in the plexiform layer, centrifugal cells that send projections through the optic nerves back to
59 the retina, and a variety of centripetal cell types that extend processes across the plexiform
60 layer and into the medulla[5]. The cortical layers of the OL, like the bipolar and granular cell

61 layers in the mammalian retina, are thought to carry out the first stages of visual information
62 processing[7], and are hence often referred to as the "deep retina".

63 To understand how OL circuits process information, it is necessary to define the functional
64 properties of their constituent neurons. In the vertebrate retina, glutamatergic photoreceptors
65 make excitatory retinotopic connections with off-bipolar cells and inhibitory connections
66 with on-bipolar cells; these bipolar cells in turn make excitatory glutamatergic connections
67 with retinal ganglion cells. Horizontal cells in the outer plexiform layer and most amacrine
68 cells in the inner granular layer receive excitatory glutamatergic inputs from photoreceptors
69 or bipolar cells, and send inhibitory GABA or glycinergic outputs to neighbouring cells in the
70 layer, leading to lateral inhibition[8]. In octopus, the main neurotransmitters in the OL are
71 glutamate, acetylcholine (ACh) and dopamine[9,10] yet the effects of these transmitters on
72 neural activity and their roles in specific neural circuits are not well understood. Indeed, the
73 receptors for these neurotransmitters, and their functional properties, remain mostly
74 unknown. This is particularly relevant since some invertebrates have an expanded inventory
75 of cys-loop ligand-gated ion channels (LGCs), with activating ligands and ion selectivity
76 distinct from the channels found in vertebrates[11-14]. Molecular characterisation of
77 neurotransmitter receptors in specific cell types is thus critical to understand how octopus
78 neural circuits work.

79 To address this question, we have initiated a neurochemical mapping of the OL of the
80 *Octopus vulgaris* 1-day post hatching (1-dph) paralarva, or hatchling. While the hatchling
81 brain is smaller, with only ~200,000 neurons, it has the same lobular structure to the adult
82 brain, including a laminar OL cortex[15,16]. Transcriptomic studies indicate that the paralarval
83 brain shares many neural classes found in older animals [9,10,17]. Moreover, paralarvae rely on
84 vision for their survival, and they exhibit robust visually guided behaviours including
85 phototaxis, colour change and prey capture[18].

86 Here we have mapped the expression of neurotransmitters and their receptors in the
87 paralarval OL. By expressing octopus ion channel genes in *Xenopus* oocytes, we have
88 characterised two ionotropic receptors from the *Octopus* visual system, including the first
89 example of a dopamine-gated cation channel as well as an anionic ACh receptor with specific
90 expression in dopaminergic neurons. Through functional imaging from paralarval brain
91 slices, we show that dopamine acts as a major excitatory neurotransmitter in the OL, while
92 ACh acts as an inhibitory neurotransmitter. This work represents the first functional
93 neurochemical characterisation of the octopus visual system and provides insights into the
94 functional properties of dopaminergic neurons and their roles in visual circuits.

95 Results

96 Neurotransmitter usage in the eye and optic lobe

97 As a first step toward generating a neurochemical map of the paralarval visual system, we
98 sought to characterise in detail the expression of all neurotransmitters in the eye and OL at
99 the single-cell level. Based on previous data that revealed the major neurotransmitters
100 expressed in the OL[9], we used RNA fluorescence *in situ* hybridisation chain reaction (HCR)
101 to probe the cellular-level expression of neurotransmitter marker genes in the photoreceptors
102 and the three layers of the OL. We used the vesicular ACh transporter (vacht) for ACh,
103 tyramine beta hydroxylase (tbh) for octopamine, the vesicular GABA transporter (vgat) for
104 GABA, tryptophan hydroxylase (tph2) for serotonin, tyrosine hydroxylase (th) for dopamine,
105 and the vesicular glutamate transporter (vglut) for glutamate.

106 We observed highly specific patterns of expression for each neurotransmitter in the paralarval
107 visual system. In the eye, we observed positive signal for none of the neurotransmitter marker
108 genes in the photoreceptors, with the exception of glutamate (Fig. 1 a-f). This indicates that

109 the photoreceptors are likely to be glutamatergic, the first time this has been shown in an
110 octopus species.

111 In the OL, we confirmed robust expression of the four OL neurotransmitters, categorising
112 them into five cell types: cholinergic (Chol: vacht^{+}), octopaminergic (Octo: tbh^{+}), exclusively
113 glutamatergic (Glut: vglut^{+}/th^{-}), exclusively dopaminergic (Dop: th^{+}vglut^{-}), and co-expressing
114 dopaminergic/glutamatergic (Dop/Glut: th^{+}vglut^{+}). Chol cells were absent from the OGL but
115 represented a moderate number of cells in the IGL (20%) and the highest proportion of cells
116 in the medulla (59%) (Fig. 1 g and i, Supplemental Fig. 1 a-c). Octo cells represented a low
117 proportion of cells overall and were found only in the OGL (10%) and IGL (4%) (Fig. 1 h
118 and i, Supplemental Fig. 1 d-f). Glut cells were found in all layers of the OL, representing 7%
119 of cells in the OGL, 32% of cells in the IGL and 55% in the medulla (Fig. 1 j and m,
120 Supplemental Fig. 2 a-c). Dop cells were the main cell type in the OGL (64%) and were also
121 detected infrequently in the IGL (6%) and medulla (2%) (Fig. 1 k, m, Supplemental Fig. 2 d-
122 f). Dop/Glut cells, which expressed both dopamine and glutamate, a cell type identified in
123 transcriptomic studies from both hatchling and adult brains[9,10], comprised the main cell type
124 in the IGL (47%) and were also found in smaller numbers in the OGL (11%) and medulla
125 (4%) (Fig. 1 l and m, Supplemental Fig. 2 g-i). GABA and serotonin markers were detected
126 in a small number of medulla neurons, whose numbers we did not quantify (Supplemental
127 Fig. 2 j, k). In summary, the OGL showed an enrichment of Dop neurons compared to other
128 layers, the IGL was a mixture of Glut, Chol and Dop/Glut cell types, and the medulla was
129 mainly a mixture of Chol and Glut cells. These data, consistent with previous studies of
130 neurotransmitter expression in the eye and OL[9,10], provide a quantitative base to correlate
131 neurotransmitter and receptor expression at the cellular level, an essential first step for
132 building functional circuit hypotheses.

133 **A dopamine-gated cation channel expressed in the optic lobe**

134 We next sought to functionally characterise neurotransmitter receptors expressed in the OL.
135 We focused on cys-loop LGCs, a diverse family of ionotropic receptors that includes the
136 GABA-A, glycine, 5-HT3, and the nicotinic ACh receptors of vertebrates as well as receptors
137 with novel ligand specificity and ion selectivity found in some invertebrate species[11-14]. We
138 identified putative *Octopus* cys-loop LGCs using comparative phylogenetics (Fig. 2 a) and
139 used previously published single-cell RNA sequencing (scRNA-seq) data [9] to focus on those
140 expressed in the OL. We expressed 41 candidate *O. vulgaris* 'cys-loop' LGCs heterologously
141 in *Xenopus* oocytes and used two-electrode voltage clamp (TEVC) recordings to detect
142 channel activity evoked by application of 18 candidate ligands. Using this approach, we
143 identified and characterised several candidate receptors activated by neurotransmitters
144 expressed in the OL (Supplemental file 1).

145 Among these putative receptors was a homomeric channel encoded by the LOC115218923
146 gene, which was activated by dopamine and other monoamines (Fig. 2 b and Supplemental
147 Fig. 3 a). Expression analysis using scRNA-seq revealed that the LOC115218923 gene is
148 expressed across the paralarval brain, in particular within cell-types of the OL (Supplemental
149 Fig. 3 b, d). In TEVC recordings of LOC115218923-expressing oocytes, we observed
150 currents in response to dopamine (EC_{50}: 7.6 μM), norepinephrine (55 μM), epinephrine (35
151 μM), serotonin (73 μM), tyramine (180 μM), and octopamine (18 mM)) (Fig. 2 c). As EC_{50}
152 for dopamine is in the μM range, this is consistent with the receptor localising to synapses, as
153 extrasynaptic receptors, such as g-protein coupled receptors (GPCRs), generally have a nM
154 EC_{50} range as they are found further away from the release sites and need to be more
155 sensitive to the ligand. LOC115218923-expressing oocytes also had the highest mean peak
156 current when exposed to dopamine, with norepinephrine and epinephrine (whose presence in
157 the OL has not been established) also showing large currents; serotonin, tyramine and

158 octopamine currents were negligible (Fig. 2 d). Interestingly, a potent metabotropic dopamine
159 receptor agonist, apomorphine [19], acted not as an agonist, but as an antagonist (IC_{50}: 7 μM,
160 Supplemental Fig. 4 a and c). To assess the ion selectivity of the LOC115218923-encoded
161 channel, we performed ion substitution experiments, comparing the shift in reversal potential
162 (ΔErev) for a sodium-free or low-chloride solution compared to the standard physiological
163 solution (ND96) with high sodium and chloride concentrations. We observed a large reversal
164 potential shift in the sodium-free solution, with little reversal shift in the low chloride-
165 solution (Fig. 2 e). Thus, LOC115218923 appears to form a dopamine-activated cation
166 channel, which we designated DopC1 (for ***dop****amine-gated* ***c****ation* channel).

167 Comparative phylogenetic analysis from diverse metazoan species indicated that DopC1 has
168 homologues throughout bilateria. In vertebrates its closest homologues are the α9/α10
169 nicotinic receptors, cation channels that are activated by ACh but not dopamine (Fig. 2 a).
170 Not only was DopC1 not activated by ACh, we found that nicotine, a potent antagonist for
171 mammalian α9/α10 receptors and agonist for other nicotinic channels, had no effect on
172 DopC1-expressing oocytes as either an agonist or antagonist (Supplemental Fig. 4 b and c).
173 We also found direct orthologs to DopC1 in other invertebrate species, including molluscs
174 (*Pomacea canaliculata, Aplysia californica,* and *Lottia gigantea*), an annelid (*Platynereis*
175 *dumerilii*), nematodes (*Caenorhabditis elegans*), and some arthropods (*Apis mellifera* and
176 *Daphnia magna,* but not *Drosophila melanogaster*). (Fig. 2 f). Expression of the DopC
177 orthologs from *Aplysia* (LOC101853763), *Apis* (LOC408525) and *Daphnia* (LOC116927457
178 and LOC116923538) in *Xenopus* oocytes also produced homomeric channels activated by
179 monoamines and not ACh (Supplemental Fig. 5 a-d). For all these channels, we found that
180 dopamine had the lowest EC_{50}, though other monoamines such as norepinephrine, serotonin
181 and tyramine also showed an EC_{50} in the μM range suggesting they may act as secondary
182 ligands (Supplemental Fig. 6 a-d). Likewise, peak current analysis on *Xenopus* oocytes

183 expressing these DopC1 orthologs indicated that dopamine, norepinephrine and epinephrine
184 had the largest peak current (Supplemental Fig. 6 e). We also found *O. vulgaris* sequence
185 within the DopC1 subfamily, but this gene (DopC2) did not form a functional homomeric
186 channel when expressed in *Xenopus* oocytes (LOC115215511, Supplemental Fig. 5 e), while
187 its message is expressed in OL cell types (Supplemental Fig. 3 c and d). Taken together, these
188 results suggest that in addition to its well-established neuromodulatory role through
189 metabotropic receptors, dopamine may act in octopus, as well as other invertebrate species, as
190 a fast excitatory neurotransmitter through ionotropic receptors.

191 Dopaminergic excitation in the optic lobe

192 To explore the possible role of dopamine as a fast excitatory transmitter in the visual system,
193 we examined the spatial expression pattern of DopC1 in the hatchling brain of *O. vulgaris,*
194 with the goal of identifying cells whose activity might be stimulated by dopaminergic
195 neurotransmission. We performed quantitative HCR using probes for DopC1, either alone
196 (Fig. 3 a and b) or co-labelled with marker genes for the major OL neurotransmitters (Fig. 3
197 e-h, Supplemental Fig. 7 a-e). In these experiments we detected no expression of DopC1 in
198 the eye (Fig. 3 a) but observed widespread expression in the OL (Fig. 3 a and b), principally
199 in the IGL and medulla. Specifically, DopC1 was expressed in 21% of OGL neurons, but in
200 72% of IGL neurons and 53% of medullar neurons (Fig. 3 b-d). In the OGL, the DopC1-
201 expressing cells disproportionately belonged to one of the minor cell types (Glut, Octo, or
202 Dop/Glut) and was rare in the main OGL cell type, Dop (Fig. 3 i, Supplemental Fig. 7 f).
203 DopC1 showed the highest expression in the IGL, where it was expressed in a majority of
204 each of the three major cell types in the IGL: 60% of Glut cells, 71% of Chol cells, and 92%
205 of Dop/Glut cells, the most common class in this layer (Fig. 3 i, Supplemental Fig. 7 g).
206 DopC1 was detected in a majority of both the major medullar cell types, namely Chol (64%
207 DopC1 expressing) and Glut (55% DopC1 expressing). Other cell types with and without

208 DopC1 represented a very low percent of cells in the medulla (1-4%; Fig. 3 i, Supplemental
209 Fig. 7 h). DopC1 was also expressed throughout the central brain but at lower levels
210 compared to the OL (Supplemental Fig. 8). To summarise, DopC1 showed relatively low
211 expression in the OGL, but made up a large proportion of cells in the IGL and medulla.

212 Since DopC1 showed high expression in the IGL and medulla, we hypothesised that
213 dopamine might act as an excitatory transmitter in these deeper layers of the OL. To test this
214 hypothesis, we performed calcium imaging on acute brain slices from 1-day *O. vulgaris*
215 paralarvae, measuring individual cell responses to exogenous dopamine (Supplemental Fig. 9
216 a). We stimulated brain slices with 100 µM dopamine, and subsequently with a high
217 potassium solution (HighK^+) to identify actively-excitable cells. We then performed image
218 analysis, and categorised their responses to dopamine as either excitation, inhibition or no-
219 response. We found that dopamine has a major excitatory role in the OL (Fig. 4 a). Moreover,
220 we found that the proportion of cells showing excitatory dopaminergic responses, and the
221 kinetics of these responses, varied across the different OL layers. For example, the OGL had
222 the lowest proportion of responding cells (44%), while the IGL and the medulla had the
223 highest (83% and 68% respectively). Inhibitory dopaminergic responses were rare in all
224 layers of the OL (≤1%), with all other recorded cells showing no response to dopamine
225 (OGL: 55%, IGL: 17%, Med: 31%; Fig. 4 b).

226 When we analysed the responses more closely, we also observed differences between the
227 layers in the kinetics of dopamine response, reflected in the slope, relative amplitude, and
228 duration. The IGL showed higher dopamine response amplitudes (relative to HighK^+
229 response), compared to the other layers, while the IGL and medulla had longer lasting
230 responses on average compared to the OGL (Fig. 4 c, Supplemental Fig. 9 b-e). The slope of
231 dopaminergic responses also varied between cells, with all layers containing both cells with
232 'shallow' slopes, indicating slow-increasing responses, as well as steeper slopes, indicating

233 fast-increasing responses (Fig. 4 d and e). The cells of the IGL showed statistically steeper
234 dopamine response slopes compared to the OGL and medulla (Games-Howell post-hoc test,
235 $p<0.0001$), and the steep, fast-rising responses most consistent with direct ionotropic
236 activation were most prevalent in the IGL (Fig. 4 f, Supplemental Fig. 9 f). Given that DopC1
237 expression is also most prevalent in the IGL (Fig. 3 d), our results are consistent with
238 dopamine acting through DopC1 as a fast excitatory neurotransmitter in this layer of the optic
239 lobe.

240 Dopaminergic neurons express acetylcholine-gated chloride channels

241 To gain insight into how dopaminergic neurotransmission in the OL is regulated, we next
242 investigated LGCs expressed in dopaminergic neurons. Analysis of scRNA-seq data[9]
243 revealed that a gene related to nicotinic ACh receptors, LOC115214201, showed high and
244 specific expression in dopaminergic clusters (Supplemental Fig. 10 a and b). Our comparative
245 phylogenetic analysis of cys-loop LGCs from metazoans placed this gene within a group of
246 anionic ACh-gated channels previously functionally characterised in the mollusc *Lymnaea*
247 *stagnalis*[20] (AChRB), and the platyhelminth *Schistosoma mansoni*[21] (Fig. 2 a). Our
248 phylogenetic analysis also found direct orthologs in other molluscs (*Aplysia californica,*
249 *Pomacea canaliculata, Lottia gigantea*), platyhelminths (*Schmidtea mediterranea*) and
250 annelids (*Platynereis dumerilii, Capitella teleta*). Despite being related to cationic nicotinic
251 ACh-gated channels, all genes within this group contain a PAR (proline-alanine-arginine)
252 motif in the pore lining region similar to that found in anion-permeable GABA-A and glycine
253 receptors (Supplemental Fig. 10 c) that has been linked to chloride selectivity[22]. Three genes
254 from octopus were found in this group.

255 To investigate the functional properties of these octopus LGCs and confirm if they act as a
256 ACh-gated chloride channels, we performed TEVC recording on *Xenopus* oocytes expressing

257 these genes homomerically. Two of them (LOC115229990 and LOC115212977) did not
258 show currents when expressed as homomeric channels in oocytes (Supplemental Fig. 11 a
259 and b). However, we successfully expressed the dopaminergic cluster-specific
260 LOC115214201 gene, hereafter referred to as AChRB1, in *Xenopus* oocytes as a homomeric
261 receptor (Fig. 5 a, and Supplemental Fig. 11 c). The AChRB1 channel showed currents in
262 response to both ACh and choline, though the EC_{50} of 1.9μM for ACh was much lower than
263 that for choline (98 μM) (Fig. 5 b). This indicates that ACh likely acts as the primary
264 endogenous ligand, and the micromolar EC_{50} for ACh is consistent with AChRB1 acting as a
265 synaptic receptor.

266 To determine the ion selectivity of AChRB1, we performed ion substitution experiments, as
267 described above. For these experiments we used the AChRB1 ortholog from *Octopus*
268 *bimaculoides,* as it expressed more robustly in oocytes compared to the *O. vulgaris* gene
269 while sharing the same ligand specificity properties (Supplemental Fig. 11 d and e). We
270 found that the AChRB1 channel showed a large and significant shift in reversal potential in
271 the low-chloride solution; in contrast, replacement of the normal buffer with a sodium-free
272 solution caused no significant shift (Fig. 5 c). Thus, octopus AChRB1 appears to function as
273 an anionic channel capable of mediating inhibitory cholinergic neurotransmission.

274 Inhibitory action of acetylcholine in the optic lobe

275 To explore the effect of AChRB1 on octopus visual circuits, we first investigated its
276 expression pattern in the brain of *O. vulgaris* 1-dph paralarva. We performed quantitative
277 HCR using probes for AChRB1 and found that this receptor is expressed in the eye (85% of
278 photoreceptor cells) and mainly the OGL/IGL of the OL (56% and 51% respectively), and in
279 a low proportion of medulla cells (4%) (Fig. 5 d-f). We also investigated the expression
280 pattern of AChRB1 in the OL in more detail by performing multiplex HCR of AChRB1 in

281 combination with marker genes for the major visual system neurotransmitters as above (Fig.
282 5 g-j, Supplemental Fig. 12 a-e).

283 Within the OGL, AChRB1 was expressed in most of the Octo cells (76%) and Dop neurons
284 (70%), the most common cell type in the layer. It was also expressed in around half of all
285 Dop/Glut OGL cells (49%). In contrast, AChRB1 was infrequently expressed in the rarer
286 Glut OGL cells (Fig. 5 k, Supplemental Fig. 12 f). In the IGL, AChRB1 was predominantly
287 in the most common cell type in this layer, the Dop/Glut cells (67%). In contrast, AChRB1
288 expression was not detected in IGL Octo cells and is only found in a low proportion of IGL
289 Chol (30%) and around half of all IGL Glut cells (44%) (Fig. 5 k, Supplemental Fig. 12 g).
290 AChRB1 was expressed in very few medulla cells (7% of Glut cells) and some central brain
291 cells (Fig. 5 k, Supplemental Fig. 12 h, Supplemental Fig. 13). To summarise, we observed
292 AChRB1 expression predominantly in three cell types: Glut photoreceptors in the eye, Dop
293 amacrine cells in the OGL, and Dop/Glut cells in the IGL.

294 Since all three cell types are potential recipients of synaptic input from cholinergic neurons in
295 the IGL and/or the medulla[23], and since scRNA-seq data indicated that cationic nicotinic
296 ACh-gated channels are not highly expressed in dopaminergic clusters (Supplemental Fig. 14
297 a), we hypothesised that ACh might act as an inhibitory neurotransmitter through AChRB1
298 within the octopus visual system. To test this, we performed calcium imaging on acute brain
299 slices from *O. vulgaris* paralarvae following acute application of ACh, using the same
300 protocol developed for dopamine. We could not test whether ACh inhibits photoreceptor cells
301 as the high potassium solution caused contraction of the eye muscles. However, we did
302 observe that ACh overall had effects, mostly inhibitory, on optic lobe cells (Fig. 6 a-e,
303 Supplemental Fig. 15). Specifically, ACh-mediated inhibition was observed in all layers of
304 the OL: 10% of OGL cells, 5% of IGL cells, and 19% of medulla cells (Fig. 6 f). Excitatory
305 responses mediated by ACh were observed in less than 2.6% of all cells in each layer

306 respectively and all other recorded cells had no response to ACh (Fig. 6 f). Observing
307 inhibition using calcium imaging requires the cell to already have increased calcium levels
308 (due to spontaneous activity), which was rare in our preparations. Thus, the proportion of
309 cells experiencing inhibition in each layer of the OL through ACh is likely underestimated.
310 However, the fact that ACh did not elicit excitatory responses, and in many cases elicited
311 robust cholinergic inhibition or no response, implies that ACh has an overall inhibitory role
312 in the OL.

313 Discussion

314 In this study, we have begun to map the molecular topography of the visual system of the
315 *Octopus vulgaris* paralarva, with the goal of linking neurotransmitters, their receptors, and
316 their physiological effects, at the cellular level. In particular, we have aimed to uncover the
317 physiological properties of the receptors for key optic lobe neurotransmitters, dopamine and
318 ACh, and to spatially localise these receptors relative to their neurotransmitter ligands within
319 the eye and optic lobe. We have used this information to generate visual circuit hypotheses,
320 which we have tested through imaging of dopamine and ACh responses in different layers of
321 the optic lobe, and gained new molecular level insights into neural circuits for visual
322 processing in octopus.

323 These experiments revealed that dopamine, perhaps unexpectedly, functions as a major
324 excitatory neurotransmitter in the optic lobe. Functional imaging of octopus brain slices
325 following application of dopamine showed increased activity in all optic lobe layers, most
326 prominently in the IGL and medulla. This activation correlates with the expression of DopC1,
327 a newly-characterised dopamine-gated cation channel found in nearly all IGL neurons, some
328 OGL neurons, and about half of medullar neurons. Moreover, while the calcium transients
329 evoked by dopamine showed varying kinetics, with slower responses consistent with GPCR-

330 mediated responses or secondarily activated neurons, the neurons in the IGL showed
331 consistently faster-increasing responses, suggesting direct activation via the ionotropic
332 DopC1 receptor. The widespread expression of dopamine in OGL and IGL neurons whose
333 axonic compartments are juxtaposed with the dendrites of DopC1-expressing neurons in the
334 plexiform layer provides anatomical support for the hypothesis that dopaminergic excitatory
335 transmission, mediated by DopC1, occurs in the optic lobe cortex.

336 Our observation that dopamine is largely excitatory in the *O. vulgaris* optic lobe was
337 surprising given a previous report[24] that cuttlefish optic lobe neurons were inhibited by
338 dopamine. While our calcium imaging experiments observed dopaminergic inhibition only in
339 very rare cases, it is possible that *Octopus* optic lobe neurons might be inhibited by dopamine
340 to a higher degree than what we observed, for example if simultaneous application of
341 dopamine across the whole slice biases the network towards excitation. Such inhibition,
342 perhaps mediated by a dopaminergic GPCR, could be detected by electrical recordings.
343 Alternatively, since octopods and decapods are separated by 250 million years of evolution, it
344 is possible that dopamine may play different roles in the cuttlefish and octopus optic lobes.
345 Although the optic lobe cell types appear to be largely conserved between octopus species
346 and between hatchlings and juveniles[9,10], the expression pattern of DopC1 in cuttlefish (or in
347 adult octopus) is not known.

348 The DopC receptor described here defines a new class of monoamine-gated cation channels,
349 with potential roles in neurotransmission in other invertebrates. Excitatory currents activated
350 by dopamine have been described previously in a gastropod mollusc, *Helisoma trivolvis*[25],
351 but the molecular identity of the channels mediating these currents was not known. Since the
352 DopC1 homologue from *Aplysia* is also monoamine-activated, we hypothesise that a DopC-
353 related channel might be responsible for this previously-described observation. While anionic
354 dopamine-gated channels have been previously identified in *C. elegans*, these channels

355 belong to a different LGC subfamily and appear to be specific to nematodes[12,13,26], in contrast
356 to the cationic DopC1 channels which are found in the genomes of many invertebrate species.
357 Our results therefore suggest that, in addition to its well-studied neuromodulatory activities
358 mediated by GPCRs, dopamine also acts as a fast excitatory neurotransmitter in many
359 invertebrate nervous systems, including that of the octopus.

360 In the context of the optic lobe circuitry, dopamine appears to play a significant role in
361 descending, excitatory pathways. Cephalopod photoreceptors have historically been thought
362 to be cholinergic[27,28]. However, recent scRNA-seq from the bobtail squid *Euprymna berryi*[29]
363 and our HCR results from *Octopus vulgaris* provide strong evidence that cephalopod
364 photoreceptors are glutamatergic. Cephalopod photoreceptors (in contrast to vertebrates) are
365 excited by light[7,28], and classical work of Young showed that these photoreceptors have large
366 presynaptic varicosities in the superficial plexiform layer that contact the dendrites of OGL
367 (and perhaps some IGL) neurons[23]. Since most OGL neurons are dopaminergic, these
368 neurons may serve to relay and/or filter depolarizing signals from the photoreceptors to the
369 dendrites of DopC1-expressing IGL neurons found deeper in the plexiform layer.
370 Dopaminergic transmission may thus play an important role in the retinotopic ON pathways
371 recently described in *O. bimaculoides* during light stimulation[7]. Moreover, since some IGL
372 neurons may receive direct, glutamatergic excitatory input from the photoreceptors as well as
373 feed-forward, dopaminergic excitation from OGL neurons, the feed-forward pathway may
374 serve to amplify the signal between the OGL and IGL, as was observed in these calcium
375 imaging experiments[7].

376 The DopC1 expressing Dop/Glut IGL neurons are likewise ideally placed to propagate ON
377 pathway excitation further into the medulla, as they can release glutamate, also an excitatory
378 neurotransmitter in *O. vulgaris* optic lobe[30], as well as dopamine. Many neurons in the
379 medulla express DopC1, and many also undergo activation by dopamine, in some cases with

380 rapid kinetics (Fig. 4 f). Since very few neurons in the medulla synthesize dopamine, the
381 dopaminergic inputs to the medulla likely come primarily from Dop/Glut neurons in the IGL.
382 We hypothesise that at least some Dop/Glut neurons may therefore correspond to the
383 centripetal neurons described by Young, and thereby serve as descending excitatory relays of
384 visual information from IGL to the medulla, akin to the bipolar cells in the vertebrate retina[8].
385 Thus, dopamine may be critical for descending feedforward circuitry from the OGL to the
386 IGL, and from the IGL to the medulla (Fig. 6 g).

387 Our results also define a role for ACh as an inhibitory neurotransmitter in the octopus optic
388 lobe. Although inhibition is intrinsically difficult to detect using calcium imaging, we
389 observed clear evidence of cholinergic inhibition in all layers of the optic lobe; in contrast,
390 we observed little evidence for cholinergic excitation despite such responses being easier to
391 detect. This correlates with previous reports that that ACh caused inhibition in the plexiform
392 layer of *O. vulgaris* adult OL slices, while nicotinic receptor agonists such as a-bungarotoxin
393 and atropine had no effect[30]. Our results establish a molecular basis for acetylcholine's action
394 as an inhibitory transmitter in octopus, which contrasts to its more familiar role as an
395 excitatory transmitter as seen in vertebrates.

396 Cholinergic inhibition correlates, particularly in the OGL and IGL, with the expression of an
397 ACh-gated anion channel, AChRB1. AChRB1 is a nicotinic receptor whose pore domain is
398 selective for anions rather than cations and is homologous to previously described ACh-gated
399 anion channels in the gastropod *Lymnaea* and the platyhelminth *Schistosoma*[20,21].
400 Interestingly, ACh-gated anion channels are also found in nematodes, but these are from
401 unrelated families of LGCs more closely related to GABA-A-like receptors[14]. Thus, AChRB-
402 like channels appear to be specifically found in Lophotrochozoan nervous systems. We note
403 that we also identified classical nicotinic cationic ACh-gated channels in *O. vulgaris*, though

404 they are not highly expressed in dopaminergic cells and may be more important in other
405 regions of the octopus brain and body.

406 Unlike dopamine and glutamate, which appear to function primarily in descending, feed-
407 forward pathways in the optic lobe, acetylcholine can be inferred to act in ascending,
408 feedback pathways. In particular, the OGL contains no cholinergic neurons, and at least some
409 of its neurons are clearly inhibited by acetylcholine. We observed widespread expression of
410 AChRB1 in the OGL, particularly in Dop and Dop/Glut cells; thus, ACh likely inhibits the
411 release of the two major excitatory neurotransmitters from the OGL, dopamine and
412 glutamate. The cholinergic neurons acting on these OGL AChRB1-expressing cells are
413 inferred to be IGL or medullar neurons with processes in the plexiform layer. In addition,
414 AChRB1 is expressed in photoreceptors, and previous reports indicate that ACh exerts
415 inhibitory effects on photoreceptor terminals in the plexiform layer. Thus, cholinergic
416 neurons from the IGL (centrifugal cells as described by Young[23]) send inhibitory feedback to
417 the photoreceptors, while cholinergic IGL/medulla neurons send inhibitory feedback to the
418 excitatory OGL neurons (Fig. 6 h).

419 Since cholinergic inhibition was also seen in the medulla, it is also possible the acetylcholine
420 may function in descending inhibitory pathways; in this context, it is worth noting that sign
421 inversion in the OFF retinotopic pathways observed by calcium imaging appears to occur
422 between the IGL and medullar layers[7]. It should be noted however that AChRB1 does not
423 show detectable expression in the medulla; thus, the cholinergic inhibition seen in medullar
424 neurons may indicate the presence of additional inhibitory ACh receptors that function in
425 medullar neurons. Alternatively, ACh may indirectly inhibit medullar neurons by inhibiting
426 its excitatory inputs from the IGL.

427 The co-expression of inhibitory AChRB channels with the excitatory neurotransmitter
428 dopamine has interesting functional implications for dopaminergic amacrine cells, the major
429 cell type in the OGL. Our results suggest that these neurons direct excitatory outputs to
430 DopC1-expressing cells (of all neurotransmitter types) in the IGL and receive inhibitory
431 inputs (via AChRB1) from cholinergic neurons in the IGL and potentially in the medulla.
432 This presents an interesting contrast with the amacrine cells of the vertebrate retina, which
433 receive excitatory inputs and make inhibitory outputs to bipolar cells in the inner nuclear
434 layer[8]. Thus, the signs of both the outputs, and some of the inputs, of octopus amacrine cells
435 are inverted relative to their vertebrate counterparts (Fig. 6 i). Nonetheless, the inhibitory
436 inputs received by octopus OGL neurons means that they, like vertebrate amacrine cells,
437 could potentially facilitate lateral inhibition within the plexiform layer through feedback
438 inhibition of excitatory output.

439 The coleoid cephalopods have become of great interest to neuroscientists due to their
440 independent evolution of intelligence and innovative behaviours. In addition to their well-
441 established differences in systems-level organisation, our work here demonstrates that
442 cephalopod and vertebrate brains are also profoundly different at the neurochemical and
443 cellular levels. As a result of evolutionary diversification of the ligand and ion selectivity of
444 ionotropic receptors, the octopus uses dopamine as an excitatory fast neurotransmitter, and
445 ACh as the major inhibitory transmitter, in the optic lobe. Likewise, fundamental components
446 of visual microcircuits, such as amacrine cells, have both input and output valences that are
447 inverted in octopus relative to those of vertebrates, even though they may carry out similar
448 computations. Going forward, it will be interesting to identify computational principles
449 shared between cephalopods and vertebrates, as well as those unique to the complex, "alien"
450 brain of the octopus.

Methods

Octopus vulgaris paralarvae

Adult male and female wild caught *O. vulgaris* were maintained and mated in the Oceanographic Center of the Canary Islands Instituto Español de Oceanografía (IEO-CSIC, Tenerife, Spain) according to Almansa et al.[31] and upon spawning embryos were shipped to Belgium. Embryos were then incubated until hatching in a closed system in the Laboratory of Developmental Neurobiology (KU Leuven), Belgium (ref). Animals used in this study were from spawnings that occurred between September 2021 and November 2024. All procedures involving adults and hatchlings were approved by the ethical board and competent authority on animal experimentation from CSIC (permit CEIBA 1377-2023 and 1610-2024) and KU Leuven (permit P080/2021), in compliance with Directive 2010/63/EU.

Octopus genomes

At the conception of this project a high-quality genome/transcriptome did not exist for *Octopus vulgaris* and thus the genome/transcriptome of *Octopus sinensis* (*ASM634580v1*) was used for designing primers for PCR and probes for HCR (more details below). *Octopus sinensis* is the most closely related octopus species to *Octopus vulgaris* and it was reported that there is only a 3.21% difference between the mitogenomes [32]. In addition, the *O. vulgaris* scRNA-seq [9] was performed on *Octopus vulgaris* 1-dph paralarval brains but was mapped to the *Octopus sinensis* genome. At later stages of the project a high-quality genome/transcriptome was published for *Octopus vulgaris* (*PRJEB61268,* [32] and was incorporated into the phylogenetic analysis.

472 ## Comparative phylogenetics of metazoan LGCs

473 ### Identifying LGCs in Octopus and diverse metazoan phyla

474 Cys-loop LGC protein sequences were identified using the PFAM domain PF02931, and the
475 following publicly available sequence datasets were selected to include species
476 representatives from all the major phyla. *Homo sapiens* (GRCh38.p14), *Danio rerio*
477 (GRCz11), and *Ciona intestinalis* (GCA_000224145.1), were included as Chordate
478 representatives. *Saccoglossus kowalewskii* (PRJNA42857) was the hemichordate
479 representative. *Strongylocentrotus purpuratus* (Spur_5.0) was the Echinoderm representative.
480 *Octopus sinensis (ASM634580v1)*, *Octopus bimaculoides (ASM119413v2)*, *Octopus vulgaris*
481 *(PRJEB61268)*, *Aplysia californica (AplCal3.0)*, *Lottia gigantea (Lotgi1)* and *Pomacea*
482 *canaliculate* (ASM307304v1) represented the Mollusca. Three octopus genomes were used
483 to ensure we didn't miss any LGCs that were not annotated correctly. Two sequences from
484 *Lymnaea stagnalis* were also included as they were functional characterized as anionic and
485 cationic ACh-gated channels[20]. *Platynereis dumerilli (GCA_026936325.1)*, *Hellobdella*
486 *robusta (Helro1)*, and *Capitella teleta (GCA_000328365.1)* were included as annelid
487 representatives. Three sequences from *Alvinella pompejana* were also included as they had
488 been previously functionally identified as glycine and proton-gated channels[33]. *Schmidtea*
489 *mediterranea* (PRJNA379262) and *Schistosoma mansoni* (PRJEA36577) were included for
490 Platyhelminths. *Drosophila melanogaster (BDGP6.46)*, *Daphnia magna (ASM2063170v1.1)*,
491 and *Apis mellifera* (Amel_HAv3.1) were included for Arthropods. *Caenorhabditis elegans*
492 (PRJNA13758) and *Brugia malayi* (PRJNA10729) were included for nematodes.
493 *Nematostella vectensis (PRJEB51373)*, and *Clytia hemisphaerica* [34] represented the
494 Cnidarians. All sequences were downloaded from Biomart [35], except for *O. vulgaris* where
495 we ran interproscan (v5.33) ourselves and *C. hemisphaerica* where we downloaded the
496 sequences from MARIMBA (http://marimba.obs-vlfr.fr/home). Jaiteh et al. [36] determined that

497 Ctenophora, Proifera and Placozoa had no LGCs in their genomes. We also included all
498 metazoan sequences from the Jaiteh et al., 2016 dataset, which included 31 representative
499 metazoan species.

500 **Alignment and tree generation**

501 LGCs have four transmembrane domains, and thus partial sequences with less than three
502 transmembrane domains were removed. Transmembrane domains were predicted using
503 TMHMM [37]. The longest isoform for each gene was manually identified and others were
504 removed. Alignment was performed using MAFFT (v7.505) with E-INS-i parameters
505 allowing for large gaps [38], as Jaiteh et al., [36], determined this was an effective approach for
506 aligning LGC protein sequences. The alignment was trimmed using Trimal (v1.4.1) gappyout
507 method [39]. The alignment was manually assessed to ensure each sequence had the 'cys-loop
508 region', and the four transmembrane domains. Any sequences with large inserts were
509 removed iteratively until a satisfactory alignment was achieved.

510 Phylogenies were generated using IQ-TREE v2.1.4_beta with 1,000 ultra-fast bootstraps [40].
511 The tree model was calculated using IQ-TREE's ModelFinder implementation according to
512 Bayesian inference criterion (BIC) and Q.yeast+F+R10 was used.

513 **Tree visualization and annotation**

514 The tree was visualized using TreeViewer [41] and species illustrations were either generated
515 by authors or sourced from Phylopic (phylopic.org) (Fig. 2 a and e). LGCs contain a
516 characteristic 'cys-loop' region in their extracellular ligand binding domain which contains
517 13 residues flanked by two cysteines that create a disulphide bond. Jaiteh et al. previously
518 characterised a 'cys-less' group of LGCs which lack these cysteines in eukaryotes (many
519 protists and a few invertebrates) [36]. We used this cys-less group to root the tree. We assigned
520 a functional annotation for the primary ligand to any subfamily where one or more sequences

521 had been previously functionally characterized in a heterologous expression system. Our
522 LGC tree, and others in the literature, split between GABA-A-like anionic LGCs and
523 Nicotinic-ACh-like cationic LGCs. However, within these anionic/cationic subfamilies some
524 exception exists and thus the ion selectivity of these exceptional cases are also highlighted
525 where functional data exists. The references associated with the functional annotations of
526 each sequence can be found in supplemental file 2. Our LGC dataset contains 1197
527 sequences, the alignment is available as supplemental file 3 and the full tree is available as
528 supplemental file 4.

529 Two-electrode voltage clamp recordings of LGCs in *Xenopus* oocytes

530 *Xenopus* laevis plasmids

531 *O. vulgaris* RNA was extracted from 15 1-dph paralarvae using Tri-reagent (Invitrogen) and
532 the Qiagen Micro kit (Qiagen). *Daphnia magna* RNA was extracted from 20 adults using Tri-
533 reagent (Invitrogen) and the Qiagen Micro kit (Qiagen). cDNA for both *O. vulgaris* and *D.*
534 *magna* was synthesised using the Superscript III RT (Invitrogen) kit, and LGC sequences
535 were amplified using Q5 polymerase (NEB, MA, USA). The cDNA sequence for the DopC1
536 gene from *Aplysia californica* (LOC101853763) and *Apis mellifera* (LOC408525) were
537 synthesised using the GeneArt Gene Synthesis Service (Thermo Fisher Scientific, Waltham,
538 MA, USA). LGC cDNA sequences from *O. vulgaris, D. magna, A. californica and A.*
539 *mellifera* were then inserted into the KSM backbone using HiFi assembly (NEB, MA, USA).
540 The KSM backbone contains *Xenopus* β-globin UTR regions and a T3 promoter. The cDNA
541 sequence of the *Octopus bimaculoides* AChRB1 (LOC106879694/XM_052969792.1) gene
542 was synthesized as a geneblock DNA fragment by IDT-DNA Inc (Coralville, IA, USA) with
543 a Kozak transcriptional start signal (GCCACC) added immediately upstream of the initial

544 methionine codon. This fragment was inserted between the two Sma I restriction enzyme
545 sites of pGEMHE [42] by Gibson assembly.

546 ***Xenopus laevis* oocytes and RNA injection**

547 Defolliculated *Xenopus Laevis* oocytes were acquired from EcoCyte Bioscience and
548 maintained in ND96 solution (in mM: 96 NaCl, 1 MgCl2, 5 HEPES, 1.8 CaCl2, 2 KCl) at
549 16°C until RNA injection. KSM plasmids were linearized with NotI, and 5'-capped cRNA
550 was synthesized *in vitro* using the T3 mMessage mMachine transcription kit (Thermo Fisher
551 Scientific, CA, USA). The pGEMHE plasmid was linearised with Eco53kI and synthesized *in*
552 *vitro* using the T7 mMessage mMachine transcription kit (Thermo Fisher Scientific, CA,
553 USA). The RNA was subsequently purified with the GeneJET RNA purification kit (Thermo
554 Fisher Scientific, CA, USA). Defolliculated *Xenopus* oocytes were individually placed in v-
555 bottom 96-well plates and injected with RNA using the Roboinject system (Multi Channel
556 Systems GmbH, Reutlingen, Germany). Each oocyte was injected with 50 nl RNA solution at
557 a concentration of 250 ng/µl-500 ng/µl, depending on the construct. Following injection, the
558 oocytes were incubated in ND96 at 16°C for 2-4 days prior to recording.

559 **Two-electrode voltage clamp recording and analysis**

560 TEVC recordings were performed either using the automated Robocyte2 system (Multi
561 Channel Systems, Reutlingen, Germany) or a manual system (OC-725D amplifier).
562 Recording electrodes for the Robocyte2 system were purchased from Multichannel systems
563 and typically had a resistance of 0.7-2 MΩ. Recording electrodes for the manual system
564 (GC120TF-10, Warner Instruments) were pulled using a P-1000 Micropipette Puller (Sutter,
565 Ca, USA) with the same resistance as above. Recording electrodes were filled with 1.5M
566 KCl and 1 M acetic acid. Oocytes were clamped at -60 mV and continuous recordings were
567 done at 500 Hz. Recordings on the Robocyte2 system were collected using the Robocyte2

568 control software and the data was extracted using the Robocyte2+ analysis software.
569 Recording on the manual system were collected using WinWCP software. The following
570 ligands were applied to all receptors described in the paper at 1mM during initial experiments
571 to determine their primary/secondary ligands. All ligands were prepared in ND96 solution
572 and were applied for 7 seconds. Fresh ND96 solution then applied for 40s to wash out the
573 ligand before applying the next ligand. The ligands used for screening were acetylcholine
574 chloride (ACh, sc-202904, Santa Cruz Biotechnology,USA), L-Glutamic acid monosodium
575 salt monohydrate (Glut, 49621, Merck, Germany), γ-Aminobutyric acid (GABA, A2129,
576 Merck, Germany), Glycine hydrochloride (Gly, G2879, Merck, Germany), dopamine
577 hydrochloride (Dop, H8502, Merck, Germany), DL-norepinephrine hydrochloride (Norepi,
578 A7256, Merck, Germany), (+/-)-Epinephrine hydrochloride (Epi, E4642, Merck, Germany),
579 Tyramine hydrochloride (Tyra, T2879, , Merck, Germany), (+/-)-Octopamine hydrochloride
580 (Octo, O0250, Merck, Germany), serotonin hydrochloride (5-HT, sc-201146A, Santa Cruz
581 Biotechnology, USA), Choline chloride (Chol, C1879, Merck, Germany), Betaine
582 hydrochloride (Bet, B3501, Merck, Germany), adenosine (Ado, 01890, Merck, Germany),
583 Adenosine 5′-triphosphate disodium salt hydrate (ATP, A26209, Merck, Germany), β-alanine
584 (β-al, 146064, Merck, Germany), D-serine (D-ser, S4250, Merck, Germany), and L-Lysine
585 (Lys, L5501, Merck, Germany).

586 Dose response analysis was performed by first perfusing the oocytes with ND96 to estimate
587 resting potential of the oocytes. Then the ligand solution was applied for 7 seconds and then
588 ND96 solution was applied again for 40 seconds to bring the oocyte back to resting potential.
589 This was repeated for all doses of the ligand from low to high concentrations. The dose
590 response results combined data from 3-7 oocytes and the data was normalised to the largest
591 current in each oocyte. Normalized mean and standard deviation where then imported into

592 GraphPad prism where data was plotted and EC_{50} values were calculated by fitting to the Hill
593 equation using three parameter slopes to obtain the highest degree of fit.

594 Ion selectivity analysis was performed using ND96 solution, a sodium-free solution (96mM
595 NMDG, 2mM KCl, 1.8mM CaCl2, 5mM HEPES, 1mM MgCl2) and a low-chloride solution
596 (96mM Na Gluconate, 2mM KCl, 1.8mM CaCl2, 5mM HEPES, 1mM MgCl2). A voltage
597 ramp from -150 mV to +30 mV was applied to oocytes expressing the receptor of interest in
598 the presence of the following solutions in the following order; ND96, ND96+ligand, sodium-
599 free, sodium-free +ligand, low-chloride, low-chloride +ligand. The EC_{50} concentration of the
600 primary ligand was used in each case, either ACh for AChRBs and dopamine for DopCs.
601 Analysis was performed using a custom python script (https://github.com/hiris25/TEVC-
602 analysis-scripts).

603 Peak current analysis was performed by exposing individual oocytes expressing specific
604 LGCs with 1mM dopamine, serotonin, norepinephrine, octopamine, epinephrine, and
605 tyramine in this order and the current was normalized to the peak current in each oocyte.
606 After exposing each oocyte to these ligands, dopamine was applied again at 1mM to ensure
607 the channel had not desensitized. The mean and standard deviation per channel and per ligand
608 were then calculated and the data was plotted in Graphpad Prism.

609 Single cell RNA sequencing analysis

610 All scRNA-seq results were from the dataset detailed in Styfhals et al [9]. Data visualisation
611 was performed in Seurat v4 [43].

612 RNA fluorescent *in situ* hybridisation chain reaction (HCR)

613 1-dph paralarvae were sedated in 2% ETOH/artificial seawater, humanely killed in 4%
614 EtOH/artificial seawater and fixed overnight in 4% paraformaldehyde (PFA) in phosphate-

615 buffered saline treated with DEPC (PBS-DEPC). RNA fluorescent *in situ* hybridization chain
616 reaction (HCR) was performed as previously described [44]. In brief, parlarvae were embedded
617 in paraffin following progressive dehydration and sectioned with a paraffin microtome
618 (Thermo Scientific, Microm HM360) to obtain 6-µm-thick transversal sections. Prepared
619 tissue slides were then used to perform hybridization chain reaction experiments (HCRv3.0).
620 Probe sets were designed with the insitu_probe_generator [45], followed by automated blasting
621 and formatting to minimize off-target hybridization with a custom script [46] and synthesised
622 by IDT (DNA oPools™, Integrated DNA Technologies). Probes were blasted against the *O.*
623 *sinensis* (PRJNA551489) or the *O. vulgaris* transcriptome (PRJEB61268) [32] to ensure
624 specificity. Each probe was tested on multiple occasions on different batches of paralarvae
625 and the expression pattern reproducible. These probes were applied at 0.9 pmol per slide.
626 Upon completion of the HCR protocol, DAPI staining was performed (32670-5MG-F,
627 Merck), slides were mounted with a cover slip (Epredia, 24 x 55 m #1) using Mowiol and
628 allowed to dry for 24 h at 18°C before being stored at 4°C until imaging. All probes
629 sequences are included in supplemental file 5.

630 **HCR image acquisition**

631 Confocal microscopy was performed using a spinning disk system (Andor BC43, Oxford
632 Instruments) with 405 nm, 562 nm, 600 nm, and 700 nm excitation lasers (respectively blue,
633 green, red and far red). Images were acquired with a 60X/1.42 NA oil-immersion objective
634 (Nikon CFI Plan Apochromat Lambda D) and an sCMOS camera (Oxford Instruments, 6.5
635 µm pixel size, 82% QE) at a 0.3 µm z-step.

636 **HCR image analysis**

637 All HCR images were prepared for publication by cropping and adjusting brightness/contrast
638 using Imaris Software (Oxford Instruments) and Fiji [47]. HCR fluorescence was not visible in

639 the plexiform layer or other neuropil regions and localised around the nuclei, therefore a
640 custom python script was written to quantify HCR fluorescence within the nuclear regions of
641 cells in the *O. vulgaris* paralarval brain (https://github.com/jboulanger/fish-octopus). The
642 expression pattern was consistent across replicates and thus quantification was performed on
643 individual slices. The cell pose pre-trained 'Nuclei' model was used to segment nuclei (DAPI
644 channel) in 3D from the Z-stack projections[48]. Each 6µm section contained ~2 layers of
645 densely packed nuclei. The Napari polygon tool was used to manually define anatomical
646 regions (i.e. OGL, IGL, Med, CB) (https://github.com/napari/napari). A difference of
647 Gaussian filter with sigma [0.5,1,1 pixels] along the z,y,x axes was used to identify positive
648 fluorescent signals from background signal. The filtering was followed by a Relu activation
649 defined as $\max\left(0, \frac{x}{s} - 4\right)$ where the standard deviation s is estimated using a maximum
650 absolute deviation to define a score. The mean fluorescence of this score for each fluorescent
651 channel within the area of the 3D segmented nuclei was recorded. A second threshold was
652 then manually defined for each gene to determine positive/negative expression within a
653 segmented nucleus.

654 Calcium imaging of acute paralarval brain slices

655 Reagents and solutions

656 Octomedia was prepared as follows; (in mM) NaCl: 214.04, $MgSO_4x7H_2O$: 26.17, KCl: 4.61,
657 NaHCO3: 2.29, $MgCl_2x6H_2O$: 28.04 , D-glucose: 38.08 $CaCl_2x2H_2O$: 10.12, and 500 ml L-
658 15, Leibowitz, with L-glutamine (Sigma, MFCD00217482). HighK^+ Octomedia is identical
659 to Octomedia except NaCl and KCl have been adjusted to 168.65 mM and 50 mM
660 respectively. Both solutions were adjusted to pH 7.6-7.7 with KOH, filtered using the corning
661 system (431098), stored at 4°C and used within one week. Calcium indicator CAL-520
662 (Abcam, UK) was prepared at 5 mM in DMSO, and stored at -20°C. Dopamine, and ACh

663 were prepared at 100 µM in Octomedia. Agarose (11AGAL0050, MP Biomedicals) with high
664 gel strength (500 g/cm²) and low gelling temperature (26°C) was prepared at 3% in
665 Octomedia and kept in a 42°C water bath until ready to use.

666 **Brain dissection, embedding and sectioning**

667 1-dph paralarvae were anaesthetised in 2% ETOH/filtered artificial seawater (FASW:) until
668 motionless (at least 5 minutes). Their brains were dissected from their bodies to ensure all
669 surrounding skin/muscle were removed. The brain was then placed in the 3% agarose
670 solution in a 35mm petri dish. The agarose was left to solidify at room temperature for 5
671 minutes and then stored on ice until vibratome sectioning (within an hour). The agarose was
672 cut to a 1cm x 1cm block and sectioned with a vibrating-blade microtome (HM 650 V,
673 Thermo Scientific, UK) with the following parameters; 200 µm slice thickness, 0.2 mm/s
674 speed, and amplitude 0.7mm. The vibratome bath was filled with cooled Octomedia. Brain
675 slices were transferred to 25mm diameter circular coverslips. A temporary well was created
676 using a plastic 3D printed cylinder made from the plastic polylactic acid (10mm height, 3mm
677 wall thickness, 18mm diameter, supplemental file 6), and petroleum jelly was placed on the
678 rim of the cylinder to create a seal to the coverslip. Each slice was then incubated in CAL-
679 520 (5µM in Octomedia) for at least 1 hour at room temperature within this temporary well.
680 The cylinder was then removed and the circular coverslip containing the slice was directly
681 transferred to the imaging chamber.

682 **Calcium imaging and perfusion**

683 Imaging was performed with an upright epifluorescent microscope (Leica DM6 B) equipped
684 with a 490/525 nm excitation/emission filter set and operated at 4-5fps, which was limited by
685 exposure time (200-250 ms). The light intensity was as low as possible, dictated by a manual
686 knob on the light source. The iris was also set as low as possible to further reduce scattered

687 light and photobleaching. Perfusion inflow and compound switching were controlled by a
688 gravity valve system (Digitimer, UK), while outflow was maintained with a peristaltic pump.
689 The imaging chamber (PH2 and RC-21BDW, Science Products) was assembled with 22x40
690 mm rectangular coverslips creating a lid. The slices were immobilised using netting
691 (hexagonal pore size: 1mm x 1.5 mm) that lay on the agarose surrounding the brain slice.

692 Slices were perfused with Octomedia for 10 minutes before imaging to acclimatise the slice
693 to the imaging chamber. The perfusion protocol during imaging was as follows; Octomedia:
694 0-90s, Ligand: 90s-135s, Octomedia: 135s-270s, HighK^+ Octomedia: 270s-end:

695 Calcium imaging analysis

696 A total of 973 cells across 17 slices were analysed during dopaminergic stimulation in the
697 OGL of the OL. Likewise, 1090 cells over 18 slices and 2298 cells over 18 slices were
698 analysed in the IGL and medulla respectively. In terms of ACh stimulation, we analysed 391
699 cells across 12 slices from the OGL, 473 cells across 12 slices from the IGL and 858 cells
700 across 12 slices from the medulla. The calcium imaging recordings of each slice were
701 processed as follows using the Suite2p GUI[49] and a custom python
702 scripthttps://github.com/A-Courtney/Octo_Dop_ACh_Ca_Imaging_2025).

703 Image registration

704 We observed deformations of the tissue slice during recording sessions, likely due to
705 muscular contractions, particularly during application of the HighK^+ solution. We assume
706 that they are caused by the oesophagus that runs through the centre of the brain and perhaps
707 muscle fibres surrounding the brain that were insufficiently removed during dissection. To
708 overcome this, image registration was performed within suite2p[49] using the non-rigid
709 registration approach and 128 x 128 pixels block size
710 (https://github.com/MouseLand/suite2p).

711 **ROI detection**

712 Regions of interest (ROIs), corresponding to cells, were detected within suite2p using an
713 anatomical detection approach. This was achieved in a semi-automated way by applying the
714 cell pose 'cyto3' model to the maximum intensity projection image of each slice[48], and the
715 ROIs were then refined manually. Then within the suite2p GUI any cells that were incorrect
716 were deleted and any cells that were missing were added manually. Out of focus regions were
717 not analysed.

718 **ROI quality control**

719 The ROIs detected using the anatomical approach described above were a combination of
720 'real' cells, 'dead' cells and 'neuropil' (fluorescence signals from local neurites). Therefore,
721 we wanted to remove the 'dead' and 'neuropil' ROIs and only analyse the 'real' cell ROIs.
722 We first wanted to understand the functional characteristics of 'cellular' ROIs vs 'neuropil'
723 ROIs, we manually defined multiple ROIs using fiji[47] from five slices from different
724 paralarvae exposed to both dopamine and ACh (Supplemental Fig. 16 a-d). Manually defined
725 'cellular' ROIs had a higher fluorescence and a circular structure. Manually defined
726 'neuropil' ROIs had a lower fluorescent signal and were found in between the 'cellular'
727 ROIs. We calculated the slopes in two second windows across the full normalised fluorescent
728 trace. Slope was calculated by using the difference in fluorescence between the start and end
729 of the time window, divided by the number of frames. We observed that 'cellular' ROIs had a
730 statistically significantly higher max slope compared to 'neuropil' ROIs (t-test, $p<0.05$,
731 Supplemental Fig. 16 e). We then used the mean+standard deviation of the neuropil max
732 slope (0.0218 normalised intensity/second) as a threshold so all traces that had a max slope
733 below this are likely a heavily neuropil contaminated ROI and were removed from
734 subsequent analysis. This threshold also filtered out 'dead' ROIs as the traces from these
735 ROIs have a downward fluorescent signal over the course of the recording due to

736 photobleaching and don't show the same characteristic responses to the ligand, HighK$^+$
737 solution or any spontaneous activity.

738 **Defining anatomical regions**

739 To analyse the functional characteristics of cells within different regions of the OL of *O.*
740 *vulgaris* paralarvae, we used Napari (https://github.com/napari/napari) to manually define
741 anatomical regions such as the OGL, IGL, medulla of the OL. The maximum intensity
742 projection of each slice was used to label these regions with the polygon tool.

743 **Ligand response categorisation**

744 The ligand response for each trace was defined as either excitation, inhibition or no-response.
745 Excitation was defined as the ligand stimulus window having a 20% higher mean
746 fluorescence compared to the baseline mean fluorescence (first 20 seconds of the recording),
747 when the full trace, including the HighK$^+$ response, was normalised using a min/max
748 approach (Supplemental Fig. 16 f shows example excitatory responses following dopamine
749 application. Inhibitory signals had to meet multiple criteria; 1. the ligand stimulus window
750 had to have a 20% decrease in mean fluorescence compared to the baseline mean value (first
751 20 seconds of the recording), when the full trace, including the HighK$^+$ response, was
752 normalised using a min/max approach, 2. inhibitory responses also needed to have a steep
753 downward slope (<-0.0099 normalised intensity/s) and, 3. the trough of the inhibition needed
754 to last at least 20 seconds. Supplemental Fig16 g shows example inhibitory responses
755 following ACh application. ROIs with 'no response' didn't meet either the excitation or
756 inhibition criteria and usually had a flat response during ligand application and a normal
757 HighK$^+$ response (Supplemental Fig. 16 f and g). Subtle differences in perfusion speed are
758 inevitable on different experimental days, and thus ligand and HighK$^+$ response windows
759 were manually defined.

760 **Dopamine slope analysis**

761 All dopaminergic excitatory responses that were identified above were then subsequently
762 analysed for their slope. Within each ROI trace the dopaminergic response had different onset
763 times, so the time window for calculating the dopamine response slope could not be fixed.
764 Instead, the dopamine application time window trace was extracted (80 second window),
765 smoothed using a rolling average over adjacent frames (4 second window), and normalized
766 using the min/max values. The slope is calculated as above, the time window was 2 seconds
767 and the slope for all 2 second periods across the stimulus time window were calculated, and
768 the max slope reliably identified the steepest slope of the dopaminergic response for each
769 ROI.

770 Statistical analysis of the slope of excitatory dopaminergic responses involved first checking
771 for normality per region (OGL, IGL and Med) using a Shapiro-Wilk test and none of the
772 groups were normally distributed ($p < 0.05$). The variances between the regions were not
773 equal (Levene's Test, $p < 0.05$) and thus Welch's ANOVA was used to determine if there was
774 a significant difference between the regions. Games-Howell post-hoc test was used to
775 determine which OL layers had statistically significant differences in their dopamine slope.

776 While only 'in-focus' cells were detected and analysed, there were still some variations in
777 how 'in-focus' a cell was. To ensure that this didn't impact our slope calculations we first
778 looked at the radius of cells, assuming cells with a larger radius were more out of focus, and
779 compared it to the slope of excitatory dopaminergic response. We performed Spearman
780 correlation and we did not observe a correlation between ROI radius and slope (R^2=-0.037,
781 p=0.0482, Supplemental Fig. 16 h). We also used variance of laplacian to calculate the
782 'sharpness' of a 30 by 30-pixel window surrounding the ROI [50] and compared it to the slope
783 of excitatory dopaminergic response. We did not observe a correlation between ROI
784 sharpness and slope (Spearman correlation, R^2=0.009, p=0.5647, Supplemental Fig. 16 i).

Figures

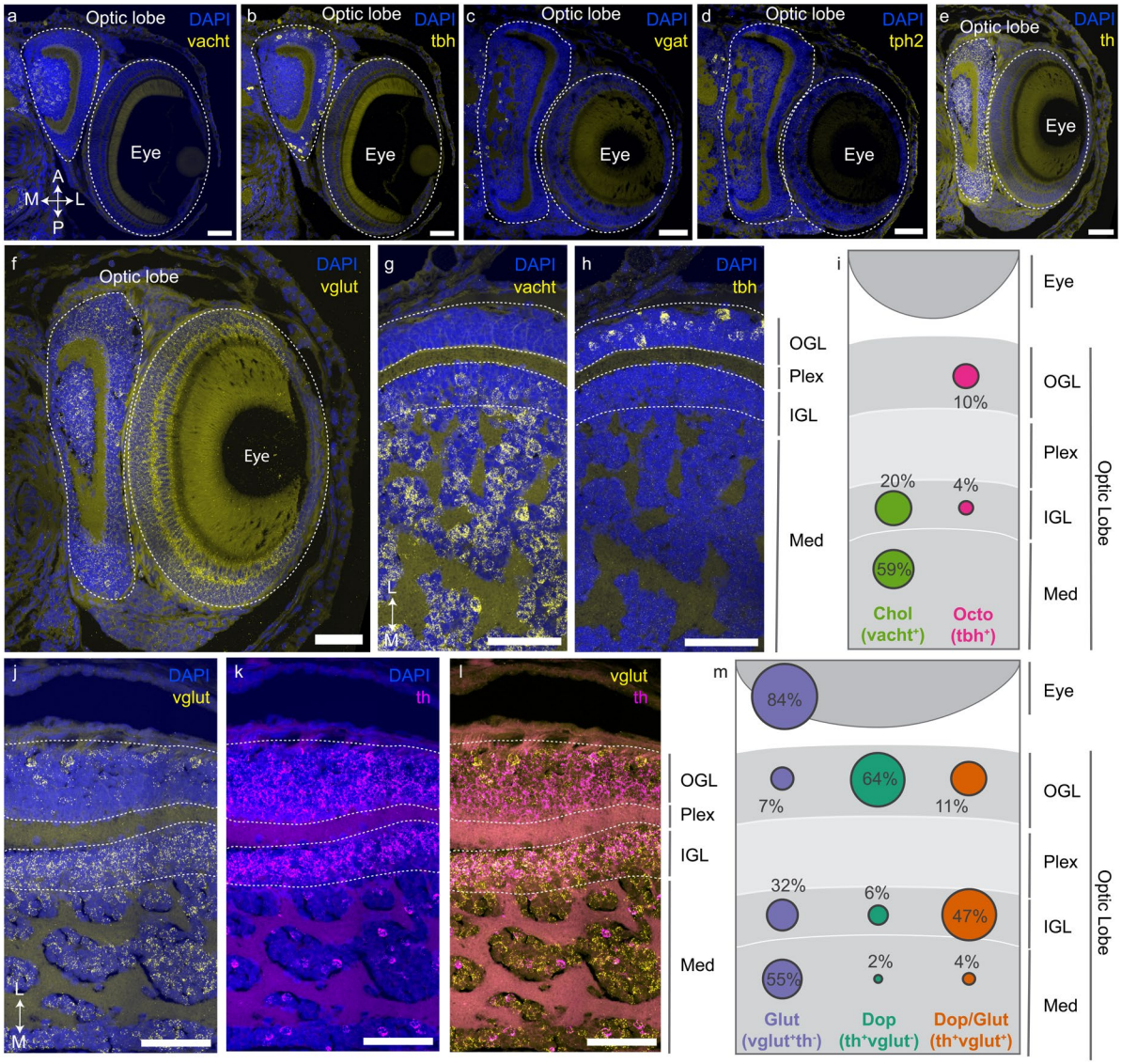

Fig. 1 Neurotransmitter cell types in the eye and optic lobe of 1-dph *O. vulgaris* paralarvae.

HCR was performed on 1-dph *O. vulgaris* head transversal sections, nuclei are visualised in blue with DAPI. Sections with both the OL and eye visible are from the ventral (towards the arms) part of the brain (see Supplemental Fig. 8 for more details). Representative HCR against vacht (cholinergic cell marker) (**A** and **G**), tbh (octopaminergic cell marker) (**B** and **H**), vgat (GABAergic cell marker) (**C**), tph2 (serotonergic cell marker) (**D**), th (dopaminergic cell marker) (**E** and **K**), and vglut (glutamatergic cell marker) (**F** and **J)** in yellow. Representative multiplex HCR against th (dopaminergic cell marker) in magenta and vglut (glutamatergic cell marker) in yellow (**L**). A summary of the HCR image quantification of Chol and Octo cell types in the eye and

OL (**I**). A summary of the HCR image quantification of Glut, Dop and Dop/Glut cell types in the eye and OL (**M**) The size of the circle represents the proportion of cells in that layer that belong to that neurotransmitter cell type. The head orientation is the same in A to F, G to M. Scale bar: 50 µm. vacht: vesicular acetylcholine transporter, tbh: tyramine beta hydroxylase, vgat: vesicular GABA transporter, tph2: tryptophan hydroxylase, th: tyrosine hydroxylase, vglut: vesicular glutamate transporter, OGL: outer granular layer, IGL: inner granular layer, Med: medulla, Plex: plexiform layer, Octo: octopaminergic cell type (tbh^{+}), Chol: cholinergic cell type (vacht^{+}), Dop: exclusively dopaminergic cell type (th^{+}vglut^{-}), Glut: exclusively glutamatergic cell type (vglut^{+}/th^{-}), Dop/Glut: exclusively dopaminergic and glutamatergic cell type (th^{+}vglut^{+}), A: anterior, P: posterior, M: medial, L: lateral.

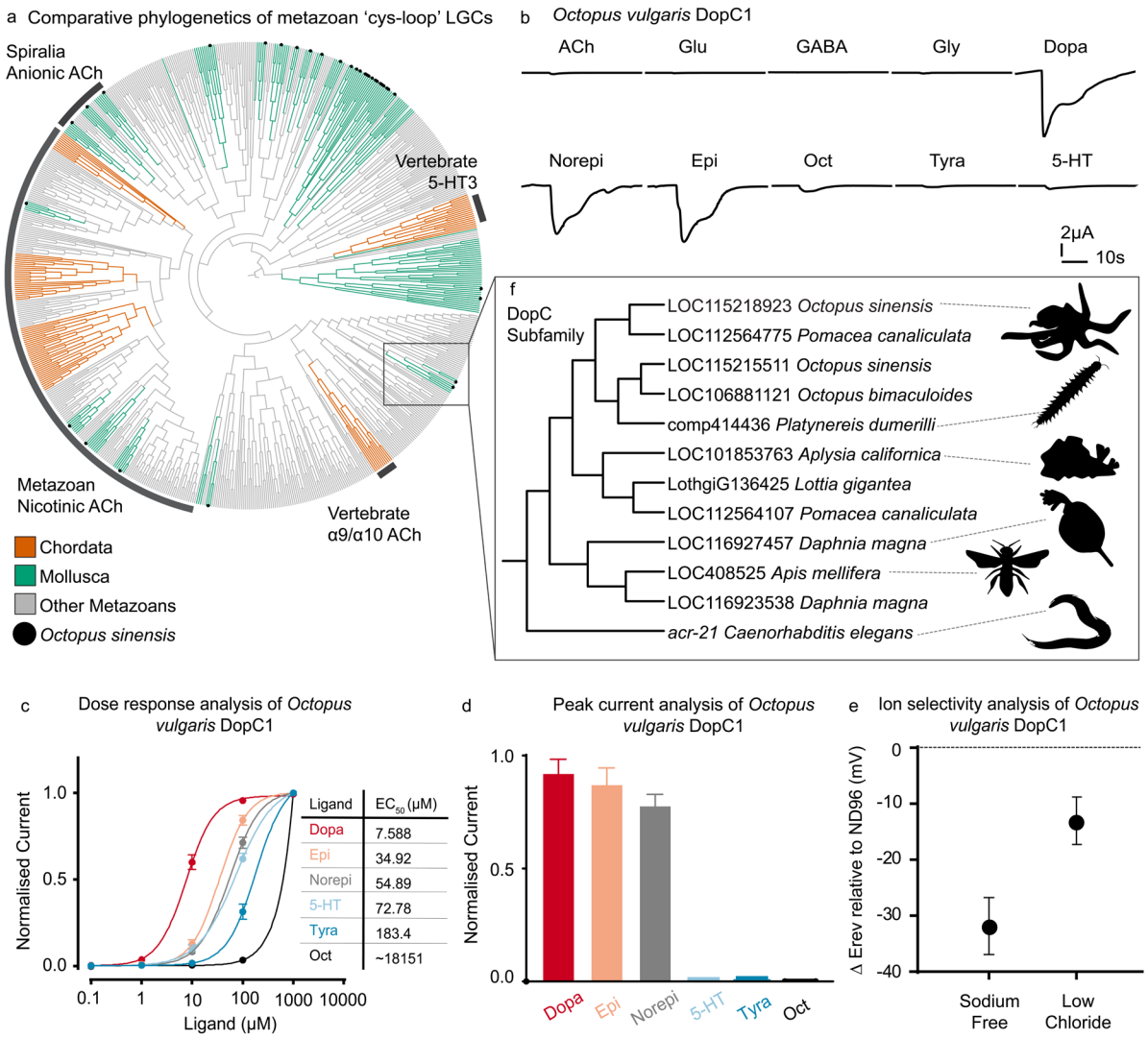

806 **Fig. 2 Discovery of a nicotinic-like dopamine-gated cation channel in *Octopus vulgaris***
807 **and other invertebrates.**

808 Comparative phylogenetics of nicotinic-like cys-loop ligand gated ion channels from major metazoan phyla (**A**).
809 Chordata sequences are highlighted in orange and molluscan sequences are highlighted in green. *Octopus*
810 *sinensis* sequences are highlighted with a black dot. Representative TEVC traces from *Xenopus* oocytes
811 expressing DopC1 from *O. vulgaris* during application of candidate ligands (**B**). Dose response analysis curves
812 for the major monoamines during TEVC recordings of *O. vulgaris* DopC1 expressed in *Xenopus* oocytes (**C**).
813 The adjacent table includes the EC_{50} values for each ligand in µM. Mean and standard error are plotted for 3-7
814 separate oocytes per ligand. The current was normalised to the max current in each oocyte. Peak current analysis
815 of *O. vulgaris* DopC1 expressed in *Xenopus* oocytes (**D**). During TEVC recordings each oocyte was exposed to
816 1mM dopamine, epinephrine, norepinephrine, serotonin, tyramine and octopamine. The mean and standard
817 deviation are plotted per ligand. The current has been normalised to the peak current in each oocyte. Ion
818 selectivity analysis of *O. vulgaris* DopC1 expressed in *Xenopus* oocytes during TEVC recordings (**E**). The
819 reversal potential (Erev, in mV) of the channel was identified during activation with 10µM (~EC_{50}) dopamine in
820 ND96, the sodium-free solution or the low-chloride solution. The difference in Erev (relative to ND96) of the
821 sodium-free solution and low-chloride solution is plotted. The mean and standard deviation are shown for 5
822 oocytes. A zoomed view of the DopC subfamily from the comparative phylogenetic analysis (**F**). ACh:
823 acetylcholine, Glu: glutamate, Gly: glycine, Dopa: dopamine, Norepi: norepinephrine, Epi: epinephrine, Oct:
824 octopamine, Tyra: tyramine, and 5-HT: serotonin, DopC1: dopamine-gated cation channel 1, ΔErev: difference
825 in reversal potential, LGC: ligand-gated ion channel.

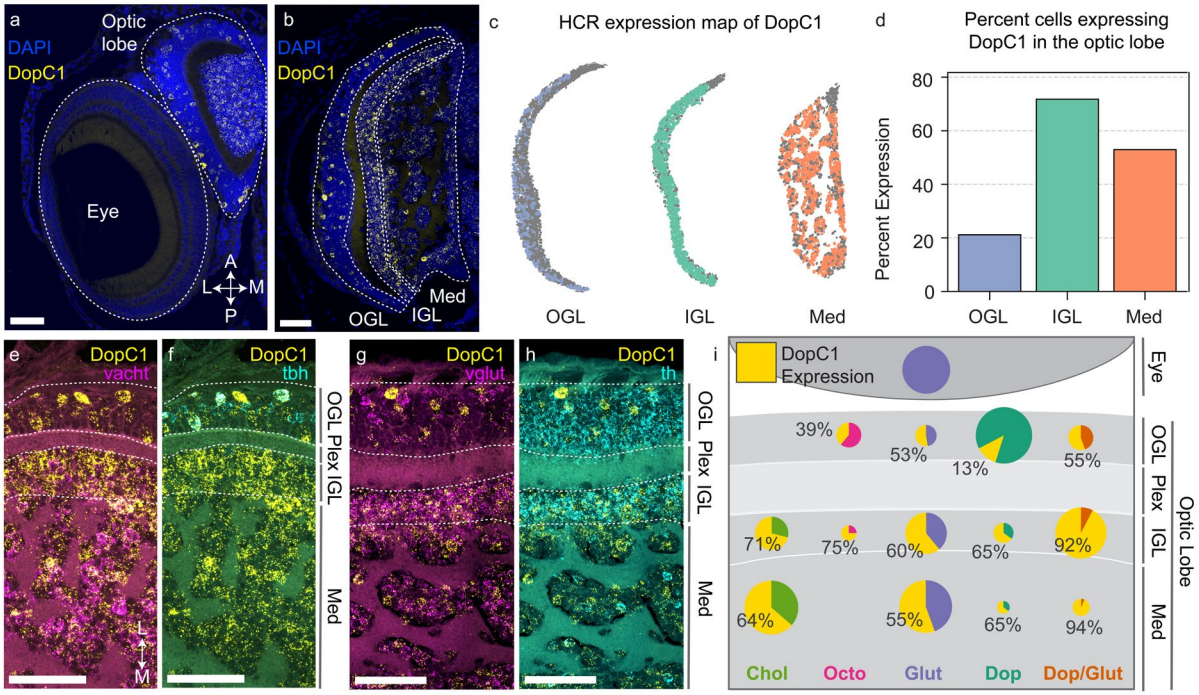

Fig. 3 DopC1 expression in the *O. vulgaris* optic lobe.

HCR was performed on 1-dph *O. vulgaris* head transversal sections and nuclei are visualised in blue with DAPI. Representative HCR against DopC1 in yellow (**A** and **B**). HCR expression maps (**C**) and barplot (**B**) showing the proportion and spatial distribution of cells expressing DopC1 in the OGL, IGL and Med of the OL, quantified from the HCR shown in **B**. Representative multiplex HCR against DopC1 in yellow and vacht (cholinergic cell marker) in magenta (**E**), tbh (octopaminergic cell marker) in cyan (**F**), vglut (glutamatergic cell marker) in magenta (**G**) and th (dopaminergic cell marker) in cyan (**H**). Summary of the expression of DopC1 in the major neurotransmitter cell types in the eye and OL (**I**). The size of the circle representatives the proportion of cells in that layer that belong to that cell type. The yellow region within each circle represents the proportion of cells of that cell type that also express DopC1. This quantification was performed on the multiplex HCRs shown in Supplemental Fig. 7. The head orientation in **A** to **C** and **E** to **I** is the same. Scale bar: 50 µm, vacht: vesicular acetylcholine transporter, tbh: tyramine beta hydroxylase, th: tyrosine hydroxylase, vglut: vesicular glutamate transporter, OGL: outer granular layer, IGL: inner granular layer, Med: medulla, Plex: plexiform layer, DopC1: dopamine-gated cation channel 1, Octo: octopaminergic cell type (tbh^+), Chol: cholinergic cell type ($vacht^+$), Dop: exclusively dopaminergic cell type (th^+vglut^-), Glut: exclusively glutamatergic cell type ($vglut^+/th^-$), Dop/Glut: exclusively dopaminergic and glutamatergic cell type (th^+vglut^+), A: anterior, P: posterior, M: medial, L: lateral.

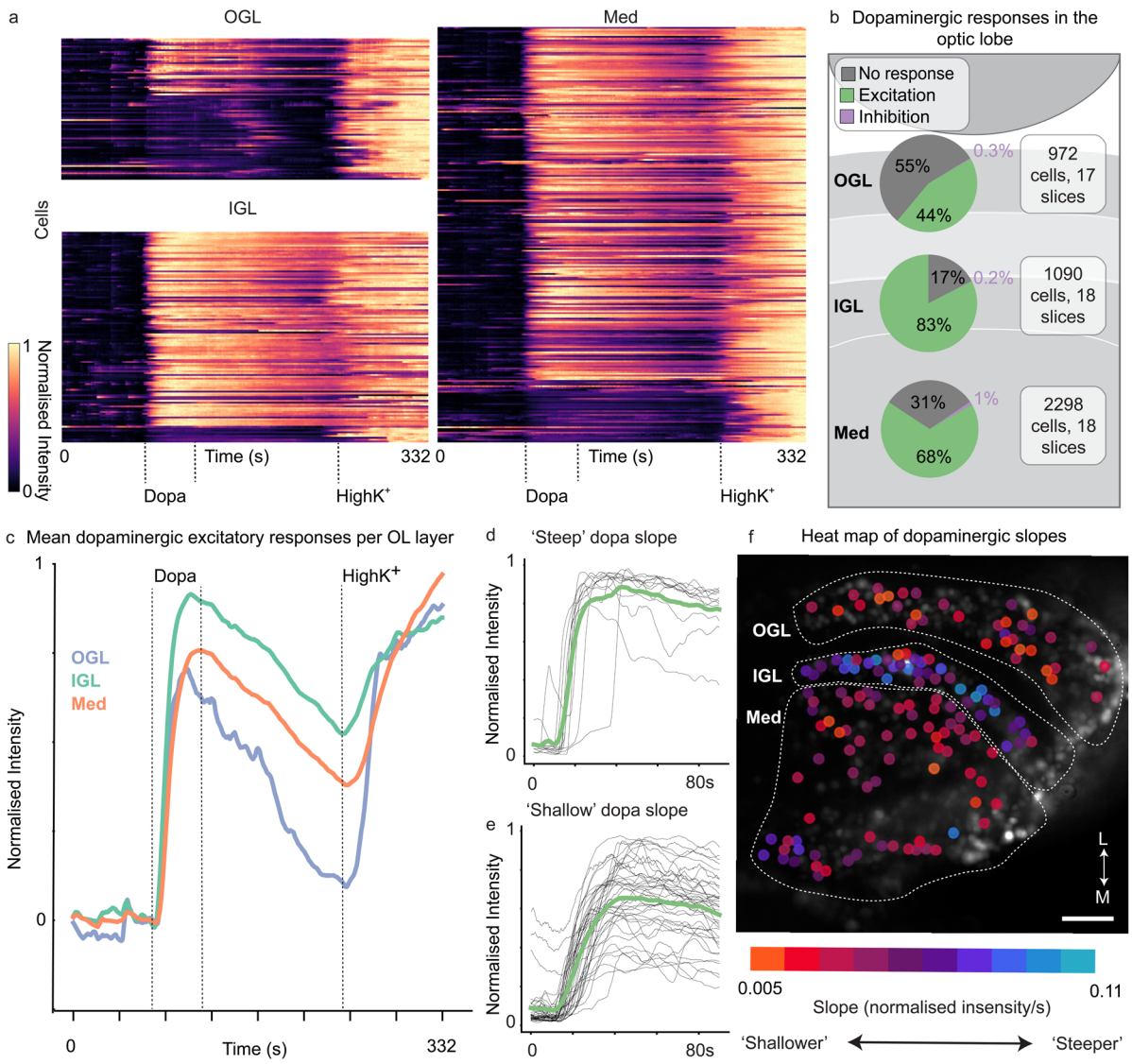

Fig. 4 Calcium imaging of 1-dph *O. vulgaris* paralarvae acute brain slices in response to dopamine.

Calcium imaging was performed on 1-dph *O. vulgaris* acute brain slices during application of 100 µM dopamine and the HighK$^+$ solution. Heat map of a representative slice during calcium imaging (**A**). The fluorescence intensity for each ROI has been smoothed using a rolling average window over 10 seconds and normalised using min/max values per ROI. Pie charts showing the proportion of cells which have dopaminergic excitation, dopaminergic inhibition or no response to dopamine, within the different layers of the OL, summed across all brain slices (**B**). Mean traces from the representative slice shown in A per OL layer (**C**). A subset of dopaminergic responses that are >0.075 (normalised intensity/s) are shown to represent 'steep' slopes (**D**). A subset of dopaminergic excitatory responses between 0.0125 and 0.0375 (normalised intensity/s) slope are

855 shown to represent 'shallow' slopes (**E**). The mean trace is shown in green. Maximum intensity projection of a
856 representative brain slice with coloured dots overlayed to generate a heat map of the slope values of the
857 excitatory dopaminergic responses in the different layers of the OL (**F**). Scale bar: 50 µm, OGL: outer granular
858 layer, IGL: inner granular layer, Med: medulla, Dopa: dopamine, HighK$^+$: high potassium solution, M: medial,
859 L: lateral.

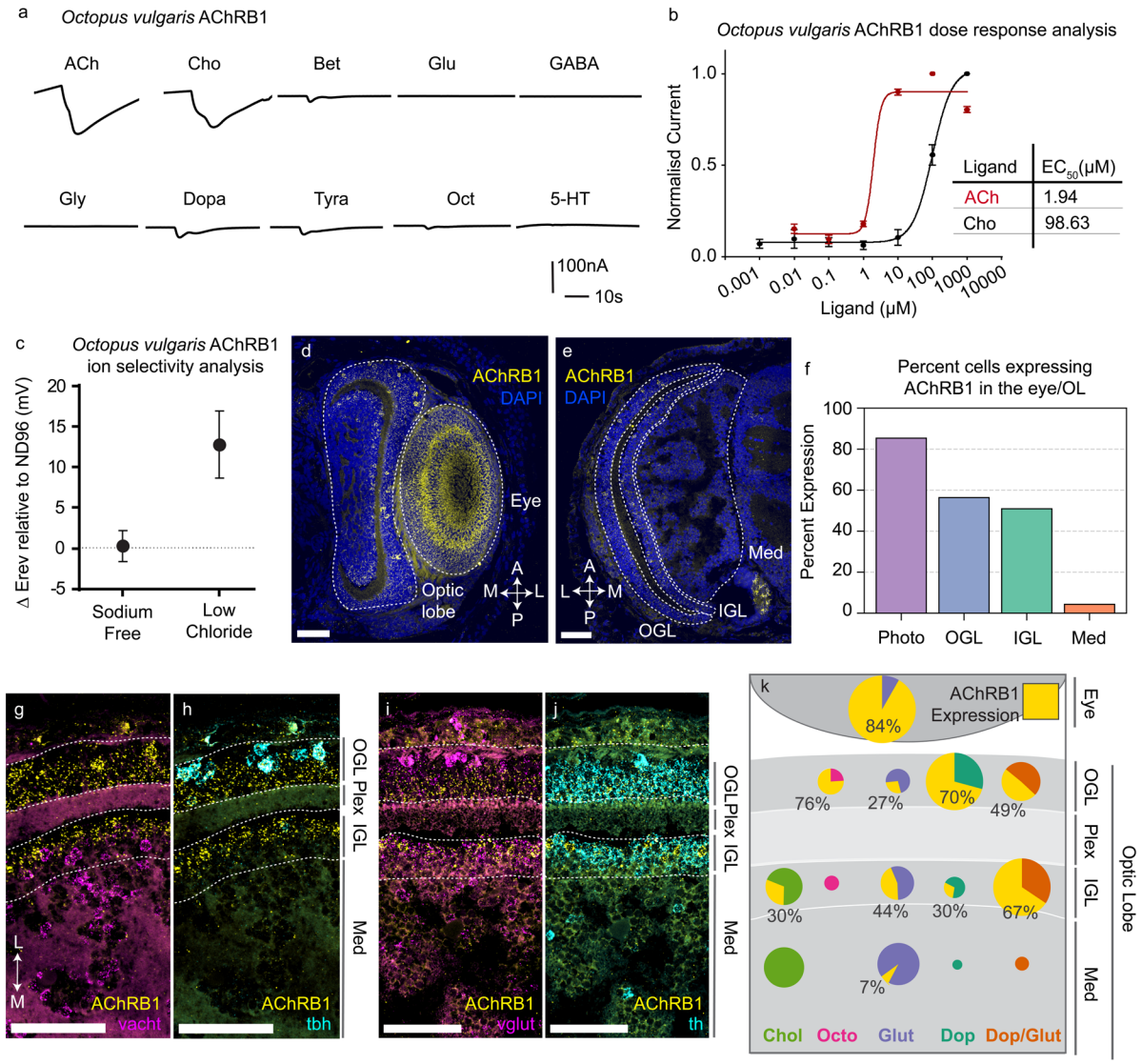

860

861 **Fig. 5 AChRB1, a ACh-gated chloride channel from *O. vulgaris*, is expressed in the**
862 **visual system**

863 Representative TEVC traces from *Xenopus* oocytes expressing AChRB1 from *O. vulgaris* during application of
864 candidate ligands (**A**). Dose response analysis curves for ACh and choline during TEVC recordings of *O.*
865 *vulgaris* AChRB1 expressed in *Xenopus* oocytes (**B**). The adjacent table includes the EC_{50} values for each

ligand in μM. Mean and standard error are plotted for 5-6 separate oocytes per ligand. The current was normalised to the max current in each oocyte. Ion selectivity analysis of *O. bimaculoides* AChRB1 expressed in *Xenopus* oocytes during TEVC recordings (**C**). The reversal potential (Erev, in mV) of the channel was identified during activation with 1μM ACh (~EC_{50}) in ND96, sodium-free solution or low-chloride solution. The difference in Erev (relative to ND96) of the sodium-free solution and low-chloride solution is plotted. The mean and standard deviation are shown for 7 oocytes. All HCRs were performed on 1-dph *O. vulgaris* head transversal sections and nuclei are visualised in blue with DAPI. Representative HCR against AChRB1 (**D** and **E**) in yellow. Barplot showing the proportion of cells expressing AChRB1 in the eye and OL, quantified from the HCR shown in D and E (**F**). Representative multiplex HCR against AChRB1 in yellow and either vacht (cholinergic cell marker) in magenta (**G**), tbh (octopaminergic cell marker) in cyan (**H**), vglut (glutamatergic cell marker) in magenta (**I**) and th (dopaminergic cell marker) in cyan (**J**). Summary of the expression of AChRB1 in the neurotransmitter cell types in the eye and OL (**K**). The size of the circle represents the proportion of cells in that layer that belong to that neurotransmitter cell type. The yellow region within each circle represents the proportion of cells of that neurotransmitter type that also express AChRB1. This quantification was performed on the multiplex HCRs shown in Supplemental Fig. 12. The orientation from G-K is the same. Scale bar: 50 μm, vacht: vesicular acetylcholine transporter, tbh: tyramine beta hydroxylase, th: tyrosine hydroxylase, vglut: vesicular glutamate transporter, OGL: outer granular layer, IGL: inner granular layer, Med: medulla, Plex: plexiform layer, ACh: acetylcholine, Cho: choline, Bet: betaine, Glu: glutamate, Gly: glycine, Dopa: dopamine, Oct: octopamine, Tyra: tyramine, and 5-HT: serotonin, AChRB: acetylcholine-gated chloride channel, ΔErev: difference in reversal potential, Octo: octopaminergic cell type (tbh^+), Chol: cholinergic cell type ($vacht^+$), Dop: exclusively dopaminergic cell type (th^+vglut^-), Glut: exclusively glutamatergic cell type ($vglut^+/th^-$), Dop/Glut: exclusively dopaminergic and glutamatergic cell type (th^+vglut^+), A: anterior, P: posterior, M: medial, L: lateral.

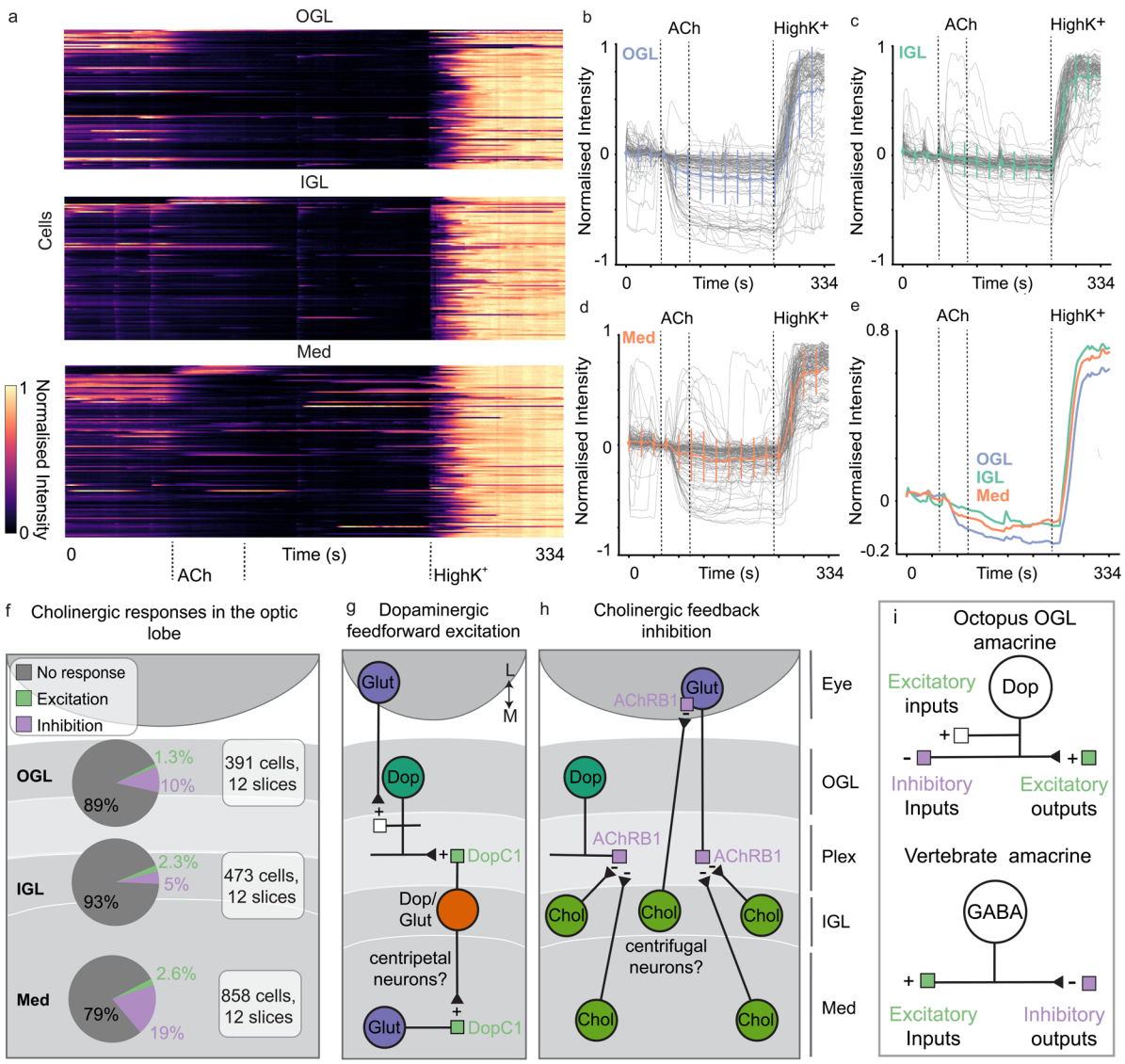

889

890 **Fig. 6 Calcium imaging of 1-dph *O. vulgaris* paralarval acute brain slices in response to**

891 **acetylcholine**

892 Calcium imaging was performed on 1-dph *O. vulgaris* acute brain slices during application of 100 µM ACh and

893 the HighK$^+$ solution. Heat map of a representative brain slice during calcium imaging (**A**). The fluorescence

894 intensity for each ROI has been smoothed using a rolling average window over 10 second periods and

895 normalised using min/max values per ROI. Normalised intensity over time for all ROIs of the representative

896 slice in A in the OGL (**B**), IGL (**C**) and Med (**D**). Mean trace and error bars are highlighted in bold. Mean trace

897 of B-D overlayed on each other (**E**). Pie charts showing the proportion of cells which have cholinergic

898 excitation, cholinergic inhibition or no response to ACh, within the different layers of the OL, summed across

899 all brain slices (**F**). Summary schematic of circuit hypothesis relating to dopaminergic feedforward excitation.

900 (**G**). Summary schematic of circuit hypothesis relating to cholinergic feedback inhibition (**H**). Schematic
901 summary of the differences between octopus OGL dopaminergic amacrine cells and vertebrate retinal
902 GABAergic amacrine cells (**I**). OGL: outer granular layer, IGL: inner granular layer, Med: medulla, Plex:
903 plexiform layer, ACh: acetylcholine, HighK$^+$: high potassium solution, AChRB1: acetylcholine-gated chloride
904 channel 1, DopC1: dopamine-gated cation channel 1, Chol: cholinergic cell type (vacht$^+$), Dop: exclusively
905 dopaminergic cell type (th$^+$vglut$^-$), Glut: exclusively glutamatergic cell type (vglut$^+$/th$^-$), Dop/Glut: exclusively
906 dopaminergic and glutamatergic cell type (th$^+$vglut$^+$), M: medial, L: lateral.

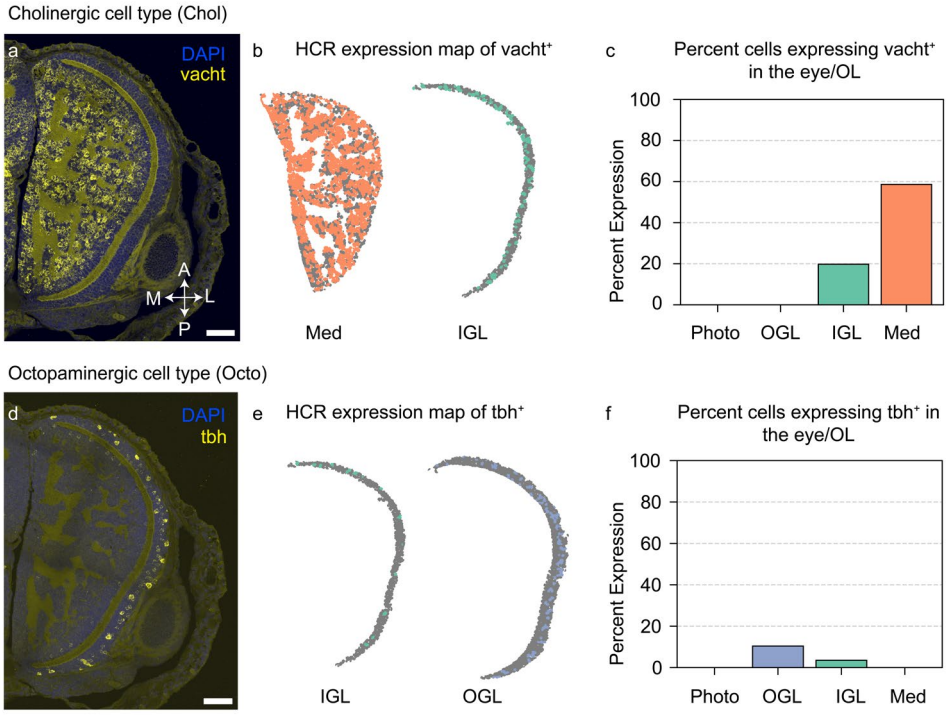

907

908 **Supp Fig. 1 Quantitative and spatial analysis of Chol and Octo cell types in the visual**
909 **system of 1-dph *O. vulgaris* paralarvae.**

910 HCRs were performed on 1-dph *O. vulgaris* head transversal sections and nuclei are visualised in blue with
911 DAPI. Representative HCR against vacht (cholinergic cell marker) in yellow (**A**). A custom python script was
912 used to quantify the expression pattern for each gene of interest within nuclear regions in the eye and OL (see
913 methods). HCR expression maps (**B**) and barplot (**C**) showing the proportion and spatial distribution of cells
914 expressing vacht in the eye/OL, quantified from the HCR shown in A. Representative HCR against tbh
915 (octopaminergic cell marker) in yellow (**D**). HCR expression maps (**E**) and barplot (**F**) showing the proportion
916 and spatial distribution of cells expressing tbh in the eye/OL, quantified from the HCR shown in D. The

orientation in A and D are the same. Scale bar: 50 µm, vacht: vesicular acetylcholine transporter, tbh: tyramine beta hydroxylase, Photo: photoreceptors, OGL: outer granular layer, IGL: inner granular layer, Med: medulla, OL: optic lobe, Octo: octopaminergic cell type (tbh^{+}), Chol: cholinergic cell type (vacht^{+}), A: anterior, P: posterior, M: medial, L: lateral.

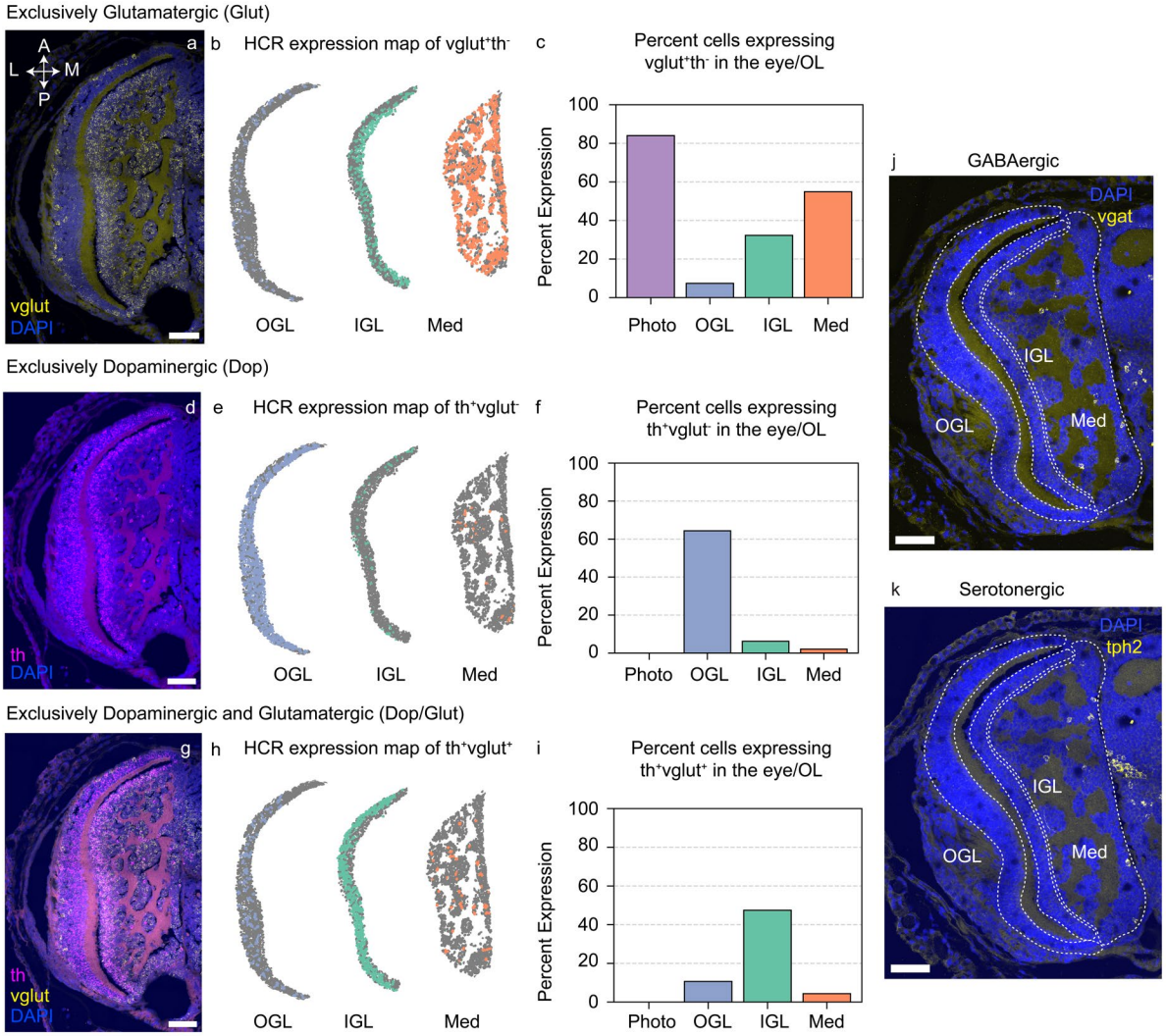

Supp Fig. 2 Quantitative and spatial analysis of Glut, Dop and Dop/Glut cell types in the visual system of 1-dph *O. vulgaris* paralarvae

HCRs were performed on 1-dph *O. vulgaris* head transversal sections and nuclei are visualised in blue with DAPI. Representative HCR against vglut (glutamatergic cell marker) in yellow (**A**). A custom python script was used to quantify the expression pattern for each gene of interest within nuclear regions in the eye and OL (see methods). HCR expression maps (**B**) and barplot (**C**) showing the proportion and spatial distribution of cells

928 expressing vglut exclusively ($vglut^{+}th^{-}$) in the eye/OL, quantified from the HCR shown in A. Representative
929 HCR against th (dopaminergic cell marker) in magenta (**D**). HCR expression maps (**E**) and barplot (**F**) showing
930 the proportion and spatial distribution of cells expressing th exclusively ($th^{+}vglut^{-}$) in the eye/OL, quantified
931 from the HCR shown in D. Representative HCR against th (dopaminergic cell marker) in magenta and vglut
932 (glutamatergic cell marker) in yellow (**G**). HCR expression maps (**H**) and barplot (**I**) showing the proportion of
933 cells expressing Dop/Glut cells ($th^{+}vglut^{+}$) in the eye/OL, quantified from the HCR shown in G. Representative
934 HCR against vgat (GABAergic cell marker) (**J**) and tph2 (serotonergic cell marker) (**K**) in yellow. All HCRs
935 have the same orientation. Scale bar: 50 µm, vgat: vesicular GABA transporter, tph2: tryptophan hydroxylase,
936 th: tyrosine hydroxylase, vglut: vesicular glutamate transporter, Photo: photoreceptors, OGL: outer granular
937 layer, IGL: inner granular layer, Med: medulla, OL: optic lobe, Dop: exclusively dopaminergic cell type
938 ($th^{+}vglut^{-}$), Glut: exclusively glutamatergic cell type ($vglut^{+}/th^{-}$), Dop/Glut: exclusively dopaminergic and
939 glutamatergic cell type ($th^{+}vglut^{+}$), A: anterior, P: posterior, M: medial, L: lateral.

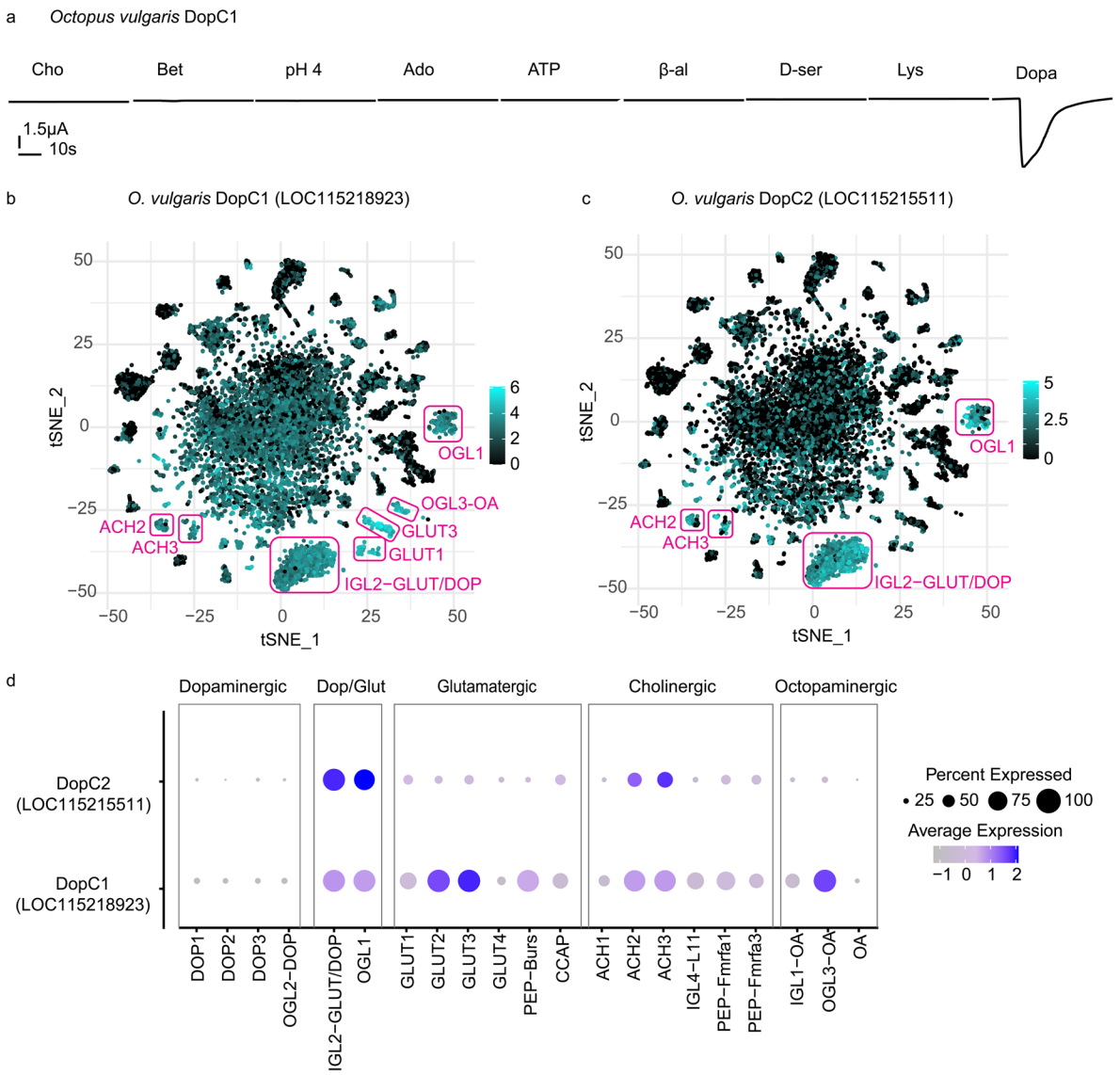

Supp Fig. 3 Additional functional and expression analysis of DopC1 from *O. vulgaris*

Representative TEVC traces from *Xenopus* oocytes expressing DopC1 from *O. vulgaris* during application of additional candidate ligands (**A**). tSNE of scRNA-seq of the *O. vulgaris* paralarval brain[9], showing the expression of the DopC1 (LOC115218923) (**B**) and DopC2 (LOC115215511) (**C**). All clusters that show high expression are highlighted in magenta. Dot plot of a subset of clusters from the single cell RNAseq of the *O. vulgaris* paralarval brain showing the expression of DopC1 and DopC2 (**D**). The size of the dots relates to the percent of cells in that cluster that express the gene, the heat map corresponds to the average expression of the gene in all cells in the cluster. DopC: dopamine-gated cation channel, Cho: choline, Bet: betaine, Ado: adenosine, ATP: adenosine triphosphate, β-al: β-alanine, Lys: lysine, Dopa: dopamine.

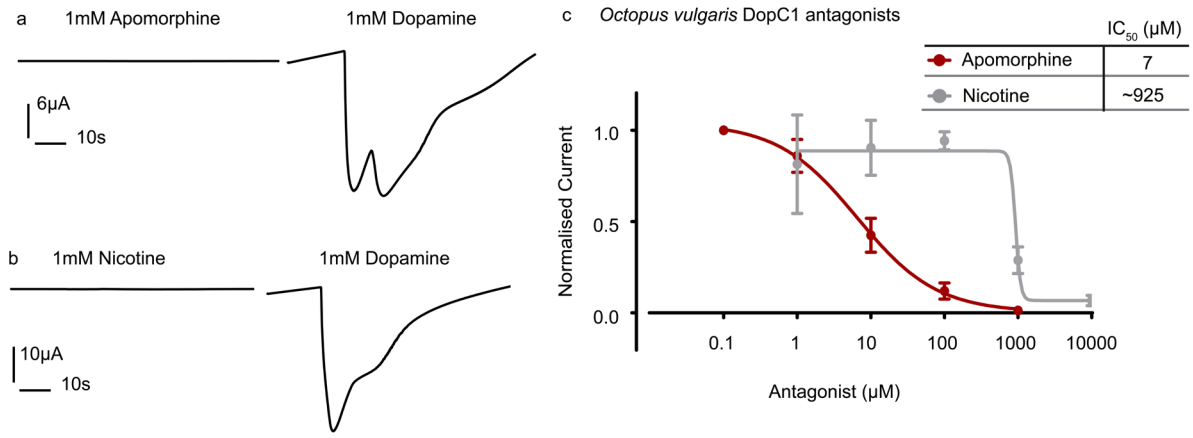

Supp Fig. 4 Characterising *Octopus vulgaris* DopC1 candidate agonists and antagonists

Representative TEVC traces from *Xenopus* oocytes expressing *O. vulgaris* DopC1 during application of apomorphine (**A**) and nicotine (**B**). Antagonistic inhibitory dose response curves from *Xenopus* oocytes expressing DopC1 from *O. vulgaris* (**C**). This was acquired by applying low to high doses of each antagonist in the presence of dopamine at 10μM (~EC_{50}). The adjacent table includes the IC_{50} values for each ligand in μM. Mean and standard error are plotted for 5-7 independent oocytes per antagonist. The current was normalised to the max current in each oocyte.

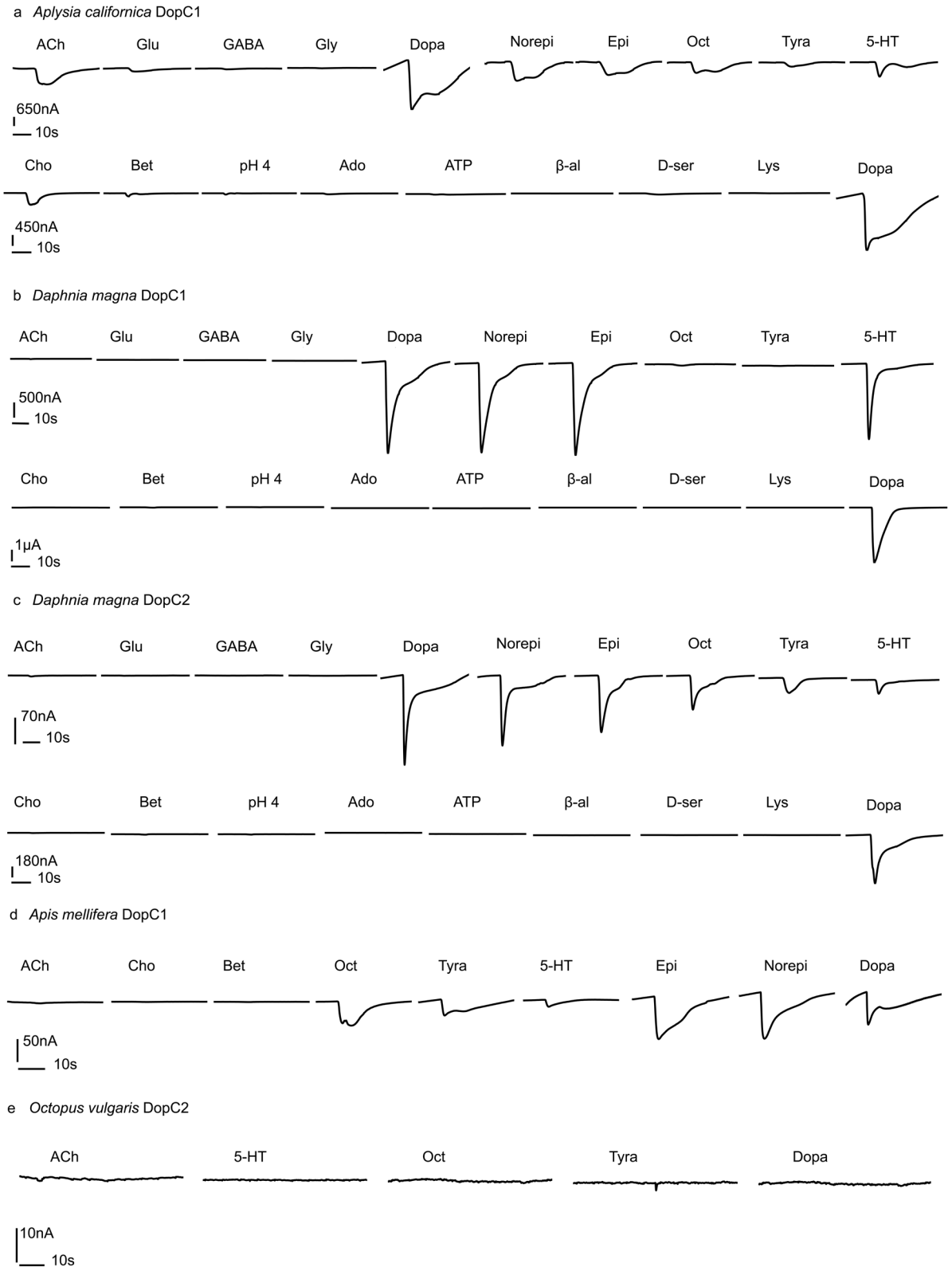
a Aplysia californica DopC1
ACh
Glu
GABA
Gly
Dopa
Norepi
Epi
Oct
Tyra
5-HT
650nA
10s
Cho
Bet
pH 4
Ado
ATP
β-al
D-ser
Lys
Dopa
450nA
10s
b Daphnia magna DopC1
ACh
Glu
GABA
Gly
Dopa
Norepi
Epi
Oct
Tyra
5-HT
500nA
10s
Cho
Bet
pH 4
Ado
ATP
β-al
D-ser
Lys
Dopa
1μA
10s
c Daphnia magna DopC2
ACh
Glu
GABA
Gly
Dopa
Norepi
Epi
Oct
Tyra
5-HT
70nA
10s
Cho
Bet
pH 4
Ado
ATP
β-al
D-ser
Lys
Dopa
180nA
10s
d Apis mellifera DopC1
ACh
Cho
Bet
Oct
Tyra
5-HT
Epi
Norepi
Dopa
50nA
10s
e Octopus vulgaris DopC2
ACh
5-HT
Oct
Tyra
Dopa
10nA
10s

959 **Supp Fig. 5 *Xenopus* oocyte TEVC recordings of DopC orthologs from *Aplysia***

960 ***californica*, *Apis mellifera* and *Daphnia magna***

961 Representative TEVC traces from *Xenopus* oocytes expressing DopC1 from *Aplysia californica* (**A**), DopC1

962 from *Daphnia magna* (**B**), DopC2 from *Daphnia magna* (**C**), DopC1 from *Apis mellifera* (**D**) and DopC2 from

963 *Octopus vulgaris* (**E**) during application of candidate ligands. ACh: acetylcholine, Glu: glutamate, Gly: glycine,

964 Cho: choline, Bet: betaine, Ado: adenosine, ATP: adenosine triphosphate, β-al: β-alanine, D-ser: D-serine, Lys:

965 lysine, Dopa: dopamine, Norepi: norepinephrine, Epi: epinephrine, Oct: octopamine, Tyra: tyramine, 5-HT:

966 serotonin, DopC: dopamine-gated cation channel.

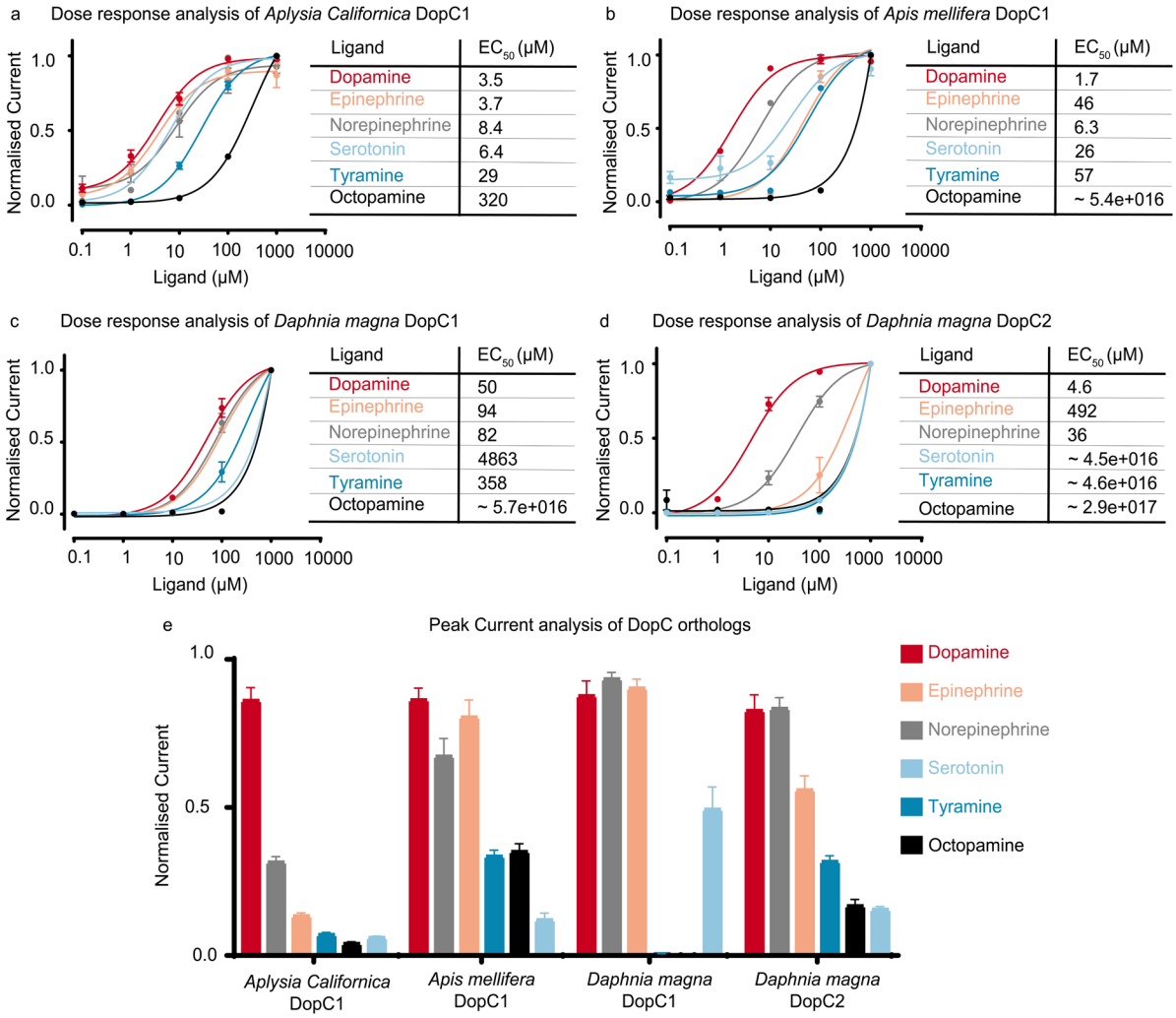

967

968 **Supp Fig. 6 Dose response and peak current analysis of DopC orthologs from *Aplysia***

969 ***californica*, *Apis mellifera* and *Daphnia magna***

970 Dose response analysis curves for the major monoamines during TEVC recordings of *Xenopus* oocytes

971 expressing DopC1 from *Aplysia californica* (**A**), DopC1 from *Apis mellifera* (**B**), DopC1 from *Daphnia magna*

972 (**C**), DopC2 from *Daphnia magna* (**D**). The adjacent table includes the EC_{50} values for each ligand in µM. Mean

973 and standard error are plotted for 3-7 separate oocytes per ligand. The current was normalised to the max current

974 in each oocyte. Peak current analysis for homomeric DopC orthologs from *Aplysia californica*, *Apis mellifera*

975 and *Daphnia magna* expressed in *Xenopus* oocytes (**E**). During TEVC recordings each oocyte was exposed to

976 1mM dopamine, epinephrine, norepinephrine, serotonin, tyramine and octopamine. The mean and standard error

977 of the mean are plotted per ligand, per receptor. The current has been normalised to the peak current in each

978 oocyte.

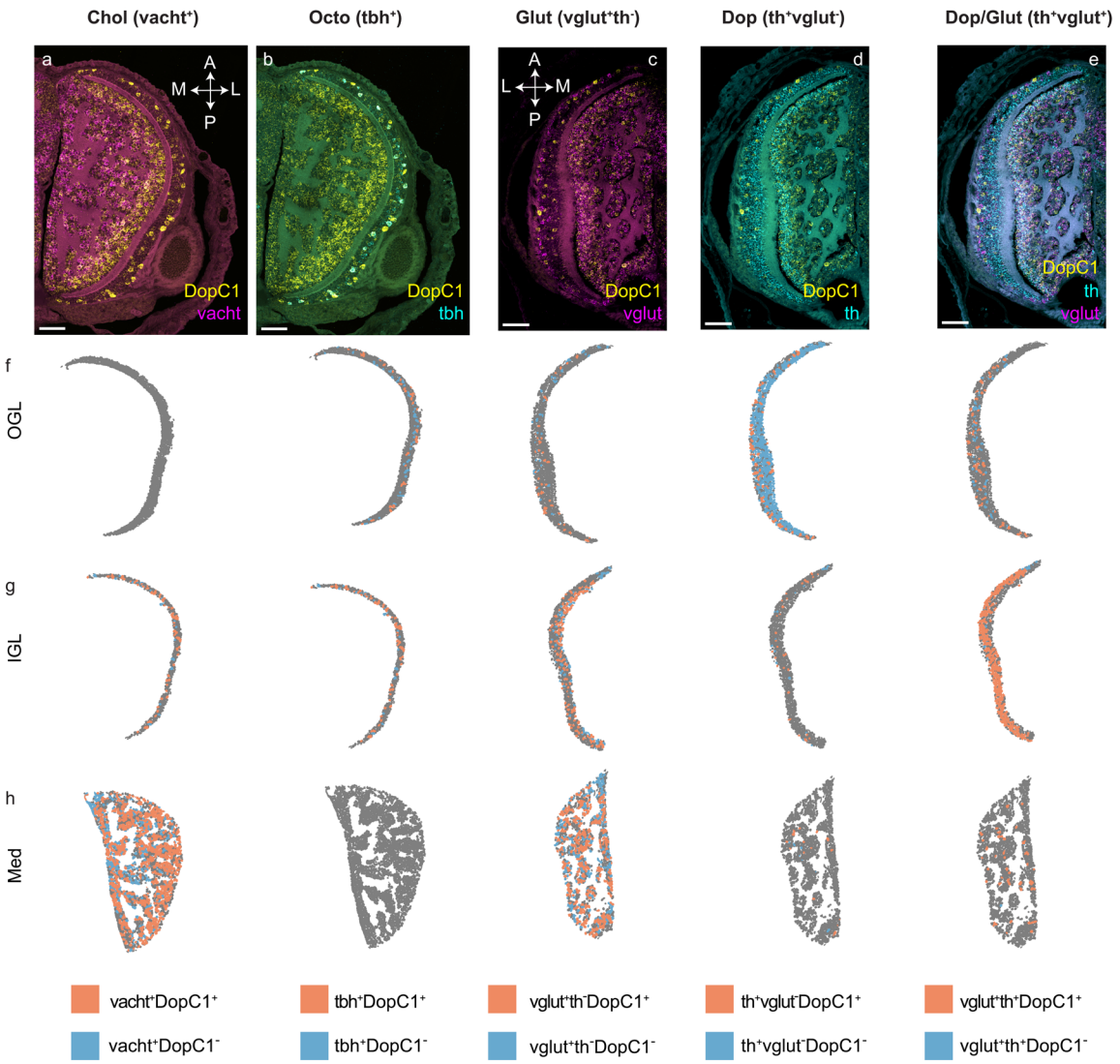

979

980 **Supp Fig. 7 Quantitative and spatial analysis of DopC1 expression in the brain of *O.***
981 ***vulgaris***

982 HCRs were performed on 1-dph *O. vulgaris* head transversal sections. Representative multiplex HCR against
983 DopC1 in yellow and vacht (cholinergic cell marker) in magenta (**A**), tbh (octopaminergic cell marker) in cyan
984 (**B**), vglut (glutamatergic cell marker) in magenta (**C**) and th (dopaminergic cell marker) in cyan (**D**).
985 Representative multiplex HCR against DopC1 in yellow, vglut (glutamatergic cell marker) in magenta (**C**) and
986 th (dopaminergic cell marker) in cyan (**E**).Representative HCR expression maps of Chol, Octo, Glut, Dop and
987 Dop/Glut cell types in the OGL (**F**), IGL (**G**) and Med (**H**) of the OL, which are positive for DopC1 (orange)
988 and negative for DopC1 (blue). The expression maps were quantified from the HCRs shown above and the
989 results are summarised in Fig. 3 i. The orientation in A and B and C-D are the same. Octo: octopaminergic cell

type (tbh$^+$), Chol: cholinergic cell type (vacht$^+$), Dop: exclusively dopaminergic cell type (th$^+$vglut$^-$), Glut: exclusively glutamatergic cell type (vglut$^+$/th$^-$), Dop/Glut: exclusively dopaminergic and glutamatergic cell type (th$^+$vglut$^+$), Scale bar: 50 µm. vacht: vesicular acetylcholine transporter, tbh: tyramine beta hydroxylase, th: tyrosine hydroxylase, vglut: vesicular glutamate transporter, OGL: outer granular layer, IGL: inner granular layer, Med: medulla, DopC1: dopamine-gated cation channel 1, A: anterior, P: posterior, M: medial, L: lateral.

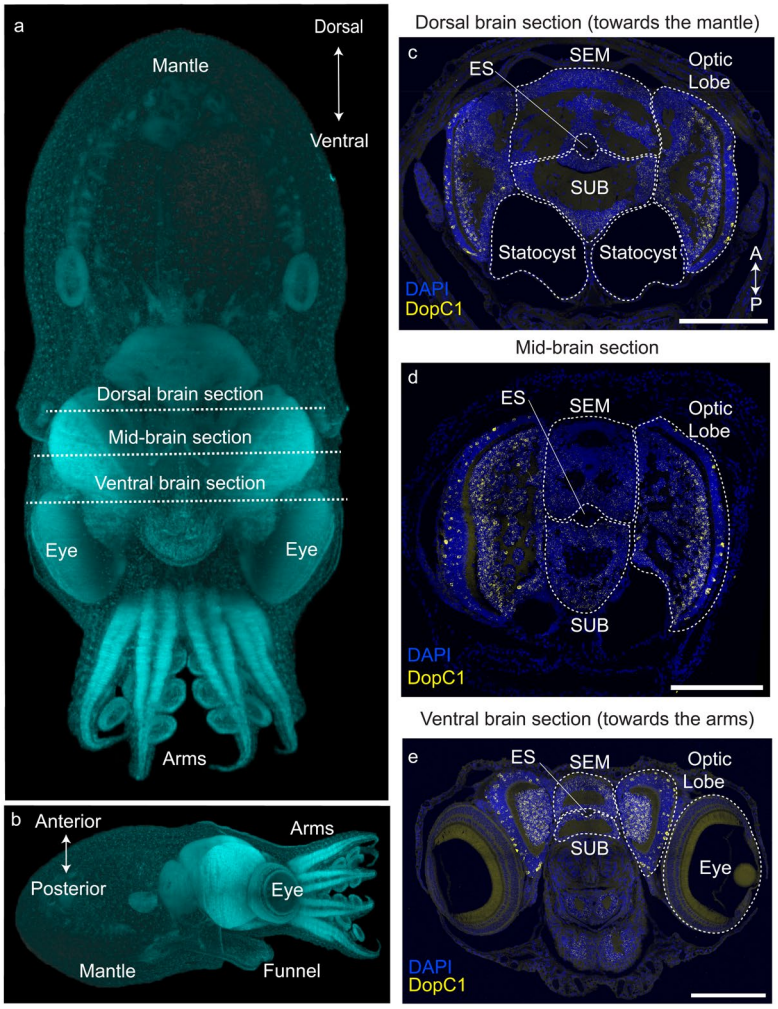

Supp Fig. 8 DopC1 expression in the central brain of *O. vulgaris* paralarvae

Maximum intensity projection of DAPI labelled 1-dph *O. vulgaris* paralarva imaged with light sheet microscopy, reproduced with permission from Deryckere et al., [51] (**A** and **B**). Representative HCR against DopC1 in yellow and nuclei (DAPI) in blue, at a dorsal position of the brain (towards the mantle) (**C**), at a mid position of the brain (**D**) and at a ventral position of the brain (towards the arms) (**E**). Scale bar: 200µm, SEM: supraesophageal mass of the central brain, SUB: subesophageal mass of the central brain, ES: oesophagus, A: anterior, P: posterior.

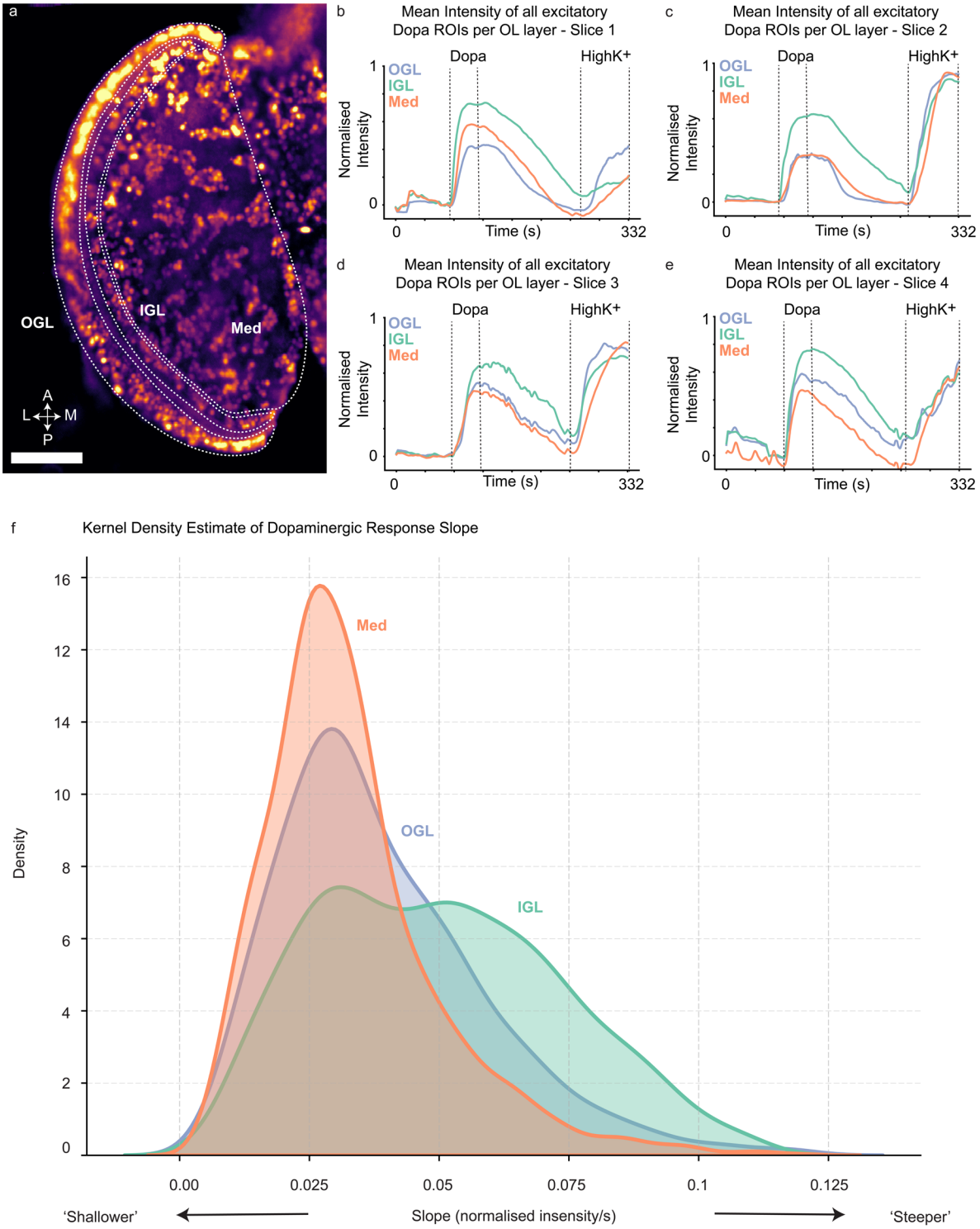
a
OGL
IGL
Med
A
L
M
P
b
Mean Intensity of all excitatory
Dopa ROIs per OL layer - Slice 1
c
Mean Intensity of all excitatory
Dopa ROIs per OL layer - Slice 2
d
Mean Intensity of all excitatory
Dopa ROIs per OL layer - Slice 3
e
Mean Intensity of all excitatory
Dopa ROIs per OL layer - Slice 4
Dopa
HighK+
OGL
IGL
Med
Normalised Intensity
Time (s)
0
332
1
f
Kernel Density Estimate of Dopaminergic Response Slope
Density
Med
OGL
IGL
0.00
0.025
0.05
0.075
0.1
0.125
'Shallower'
Slope (normalised insensity/s)
'Steeper'

1003

1004 **Supp Fig. 9 Additional analysis of calcium imaging on acute brain slices from *O.***

1005 ***vulgaris* paralarvae during application of dopamine**

1006 Calcium imaging was performed on acute brain slices from 1-dph *O. vulgaris* paralarvae. Maximum intensity

1007 projection of a representative brain slice used for calcium imaging (**A**). The mean intensity over time for all

1008 ROIs in each OL layer that were categorised as having an excitatory dopaminergic response are plotted as

1009 purple (OGL), green (IGL) and orange (Med) lines. Four different slices have been plotted (**B-E)**. Kernel

1010 density estimate of dopaminergic response slope per OL layer (**F**). Scale bar: 100 µm, Dopa: dopamine, HighK^+:

1011 high potassium solution, OGL: outer granular layer, IGL: inner granular layer, Med: medulla, A: anterior, P:

1012 posterior, M: medial, L: lateral.

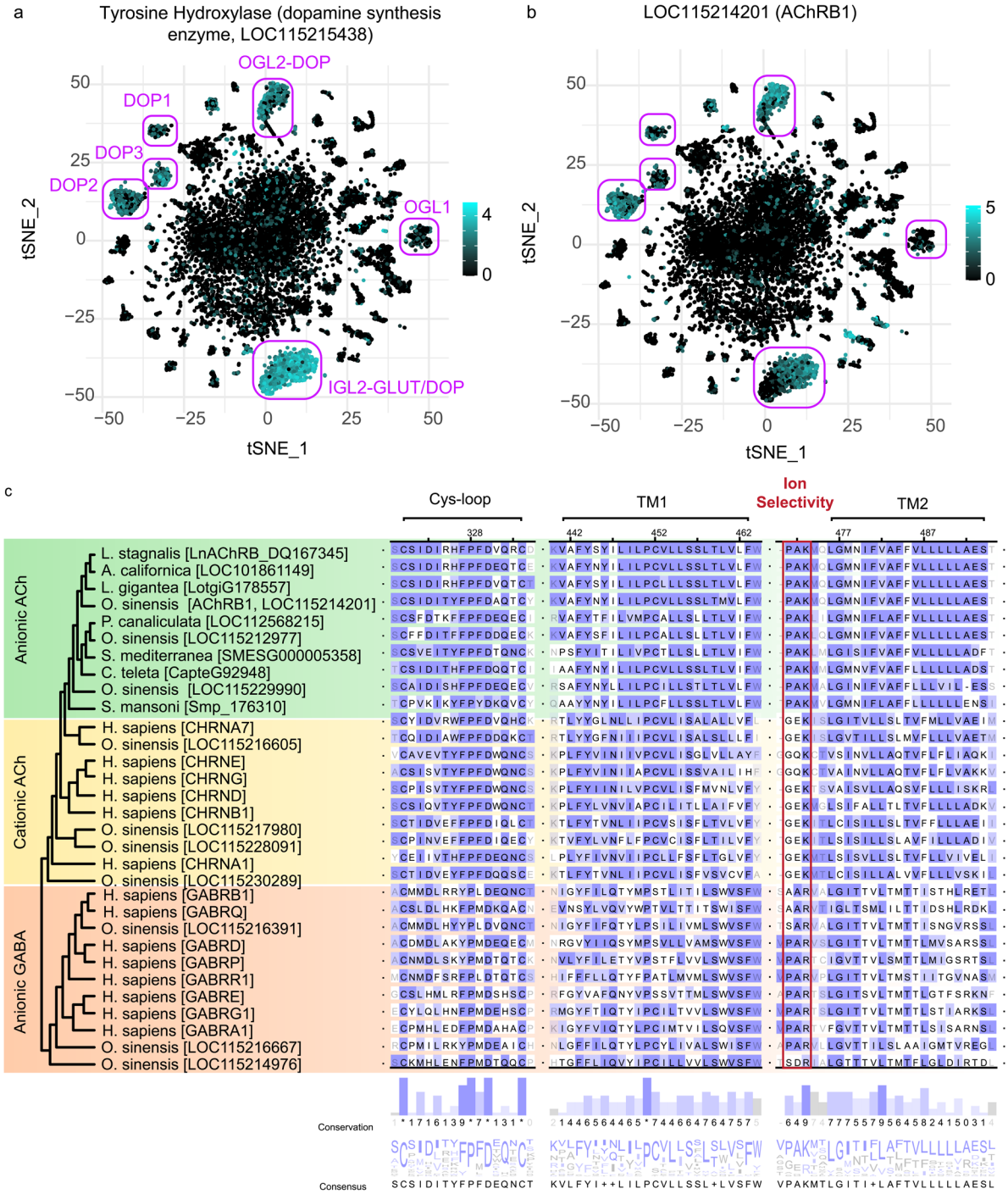

Supp Fig. 10 Additional expression, and sequence analysis of AChRB1 from *O. vulgaris*

tSNE of scRNA-seq of the *O. vulgaris* paralarval brain from[9], showing the expression of th (dopamine synthesis enzyme, LOC115215438) (**A**) and AChRB1 (LOC115214201) (**B**). Dopaminergic clusters are highlighted in magenta. Trimmed amino acid alignment showing a subset of anionic ACh, cationic ACh and anionic GABA LGCs highlighting multiple functional domains including the cys-loop region, transmembrane domain 1, the ion

1019 selectivity region and transmembrane domain 2 (**C**). Amino acid consensus and conservation values are shown
1020 below. Purple shading indicates BLOSUM62 scores indicating evolutionary divergence of individual sites. TM:
1021 transmembrane, AChRB: acetylcholine-gated chloride channel.

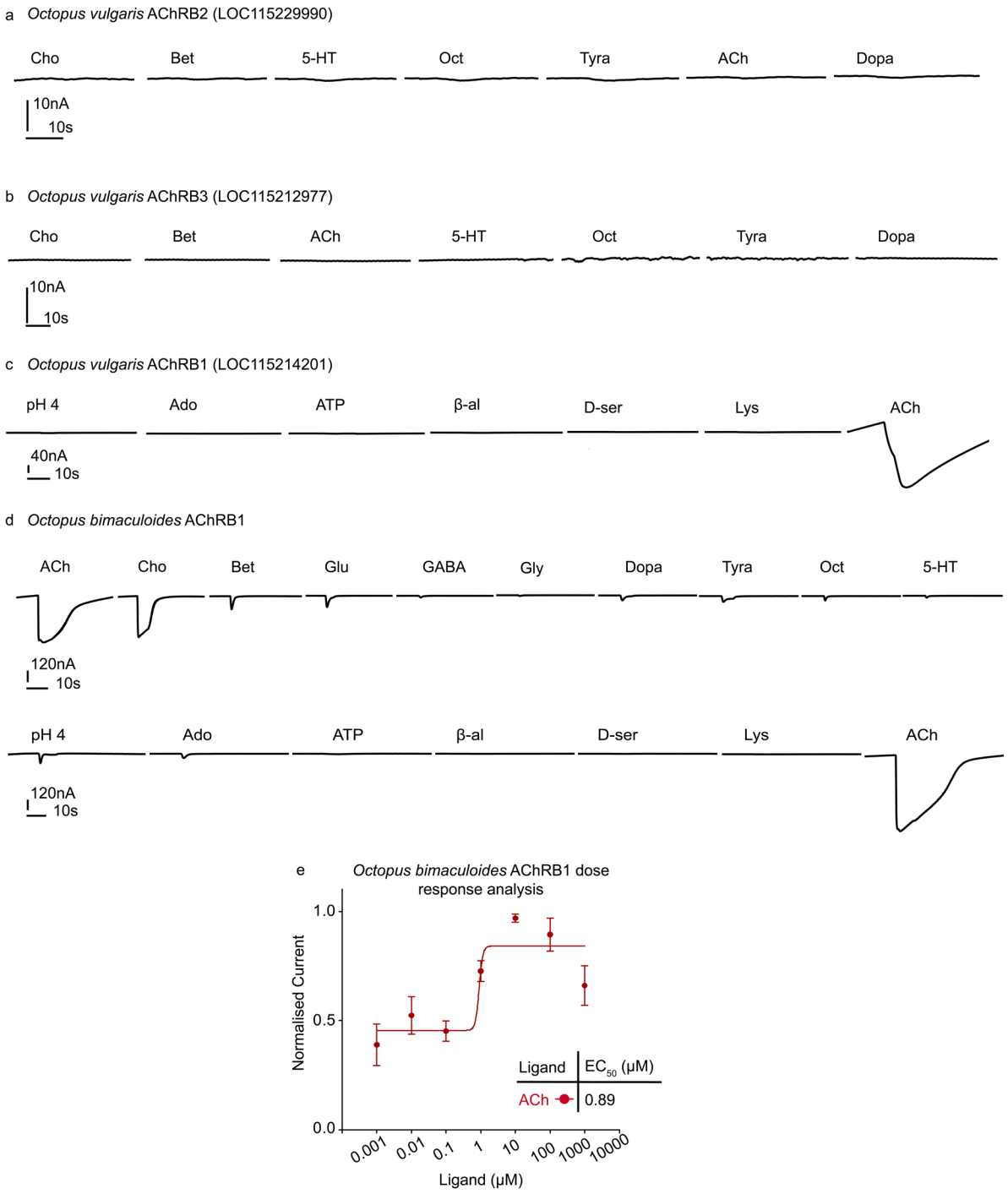

1022

1023 **Supp Fig. 11 Functional characterisation of AChRB orthologs from *O. vulgaris* and *O.***

1024 ***bimaculoides***

1025 Representative TEVC traces from *Xenopus* oocytes expressing *O. vulgaris* AChRB2 (**A**), *O. vulgaris* AChRB3

1026 (**B**), *O. vulgaris* AChRB1 (**C**), and *O. bimaculodes* AChRB1(**D**) during application of all candidate ligands.

1027 Dose response analysis curves for *O. bimaculoides* AChRB1 in response to ACh (**E**). For **D** the top and bottom

1028 traces were from separate oocytes. This was acquired by performing TEVC recordings on *O. bimaculoides*

1029 *AChRB1* expressed in *Xenopus* oocytes from low to high concentrations. The adjacent table indicates the EC_{50}

1030 values for ACh in µM. Mean and standard error of the mean are plotted for 8 separate oocytes per ligand. The

1031 current was normalised to the max current in each oocyte. ACh: acetylcholine, Chol: choline, Bet: betaine, Glut:

1032 glutamate, Gly: glycine, Ado: adenosine, ATP: adenosine triphosphate, β-al: β-alanine, Lys: lysine, Dop:

1033 dopamine, Norepi: norepinephrine, Epi: epinephrine, Octo: octopamine, Tyra: tyramine, 5-HT: serotonin,

1034 AChRB: acetylcholine-gated chloride channel.

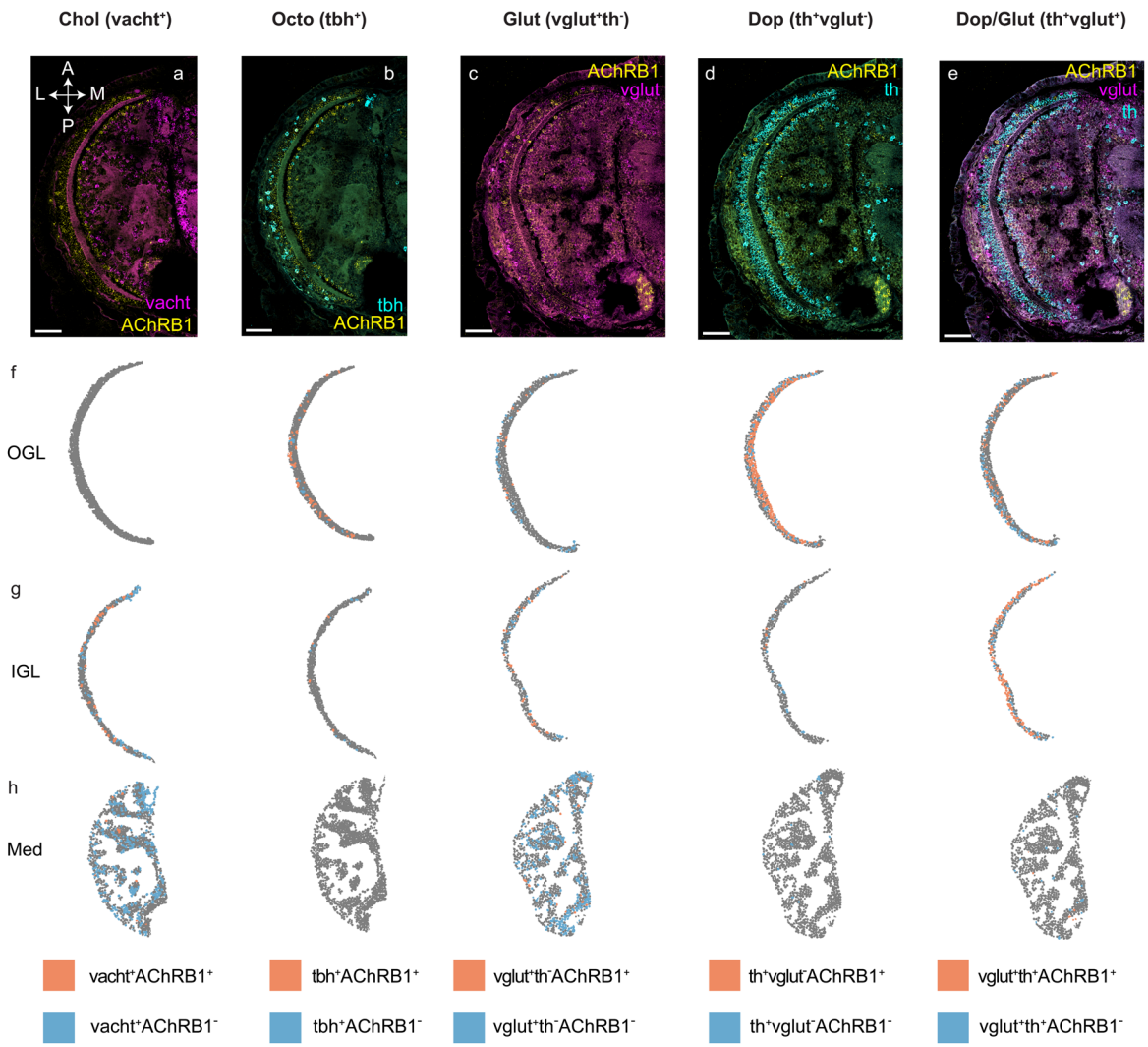

Supp Fig. 12 Quantitative and spatial analysis of AChRB1 expression in the brain of *O. vulgaris*

HCRs were performed on 1-dph *O. vulgaris* head transversal sections. Representative multiplex HCR against AChRB in yellow and vacht (cholinergic cell marker) in magenta (**A**), tbh (octopaminergic cell marker) in cyan (**B**), vglut (glutamatergic cell marker) in magenta (**C**) and th (dopaminergic cell marker) in cyan (**D**). Representative multiplex HCR against AChRB in yellow, vglut (glutamatergic cell marker) in magenta (**C**) and th (dopaminergic cell marker) in cyan (**E**).Representative HCR expression maps of Chol, Octo, Glut, Dop and Dop/Glut cell types in the OGL (**F**), IGL (**G**) and Med (**H**) of the OL, which are positive for AChRB (orange) and negative for DopC1 (blue). The expression maps were quantified from the HCRs shown above and the results are summarised in Fig. 5 k. The orientation of all HCRs is the same. Octo: octopaminergic cell type

1046 (tbh^{+}), Chol: cholinergic cell type (vacht^{+}), Dop: exclusively dopaminergic cell type (th^{+}vglut^{-}), Glut:
1047 exclusively glutamatergic cell type (vglut^{+}/th^{-}), Dop/Glut: exclusively dopaminergic and glutamatergic cell type
1048 (th^{+}vglut^{+}), Scale bar: 50 µm. vacht: vesicular acetylcholine transporter, tbh: tyramine beta hydroxylase, th:
1049 tyrosine hydroxylase, vglut: vesicular glutamate transporter, OGL: outer granular layer, IGL: inner granular
1050 layer, Med: medulla, A: anterior, P: posterior, M: medial, L: lateral, AChRB: acetylcholine-gated chloride
1051 channel.

1052 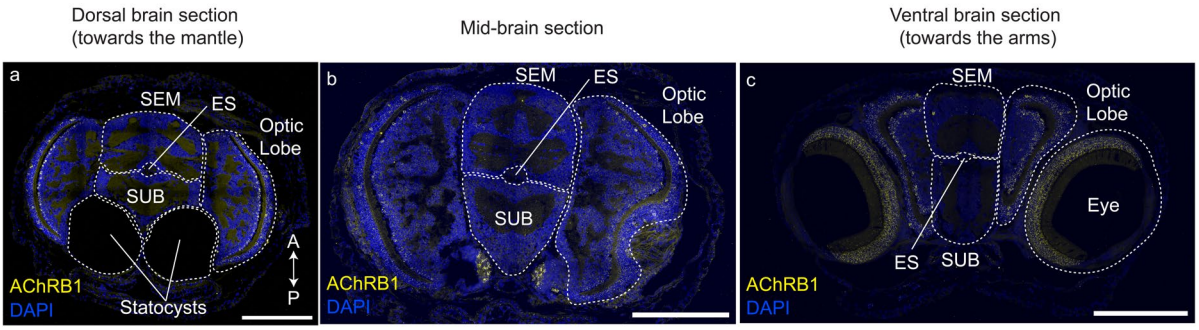

1053 **Supp Fig. 13 AChRB1 expression in the central brain of *O. vulgaris* paralarvae**

1054 Representative HCR against AChRB1 in yellow and nuclei (DAPI) in blue, at a dorsal position of the brain
1055 (towards the mantle) (**A**), at a mid-brain position (**B**) and at a ventral brain position (towards the arms) (**C**). For
1056 more details on ventral/dorsal orientations of the paralarvae see Supplemental Fig. 8. Scale bars: 200µm, SEM:
1057 supraesophageal mass of the central brain, SUB: subesophageal mass of the central brain, ES: oesophagus.

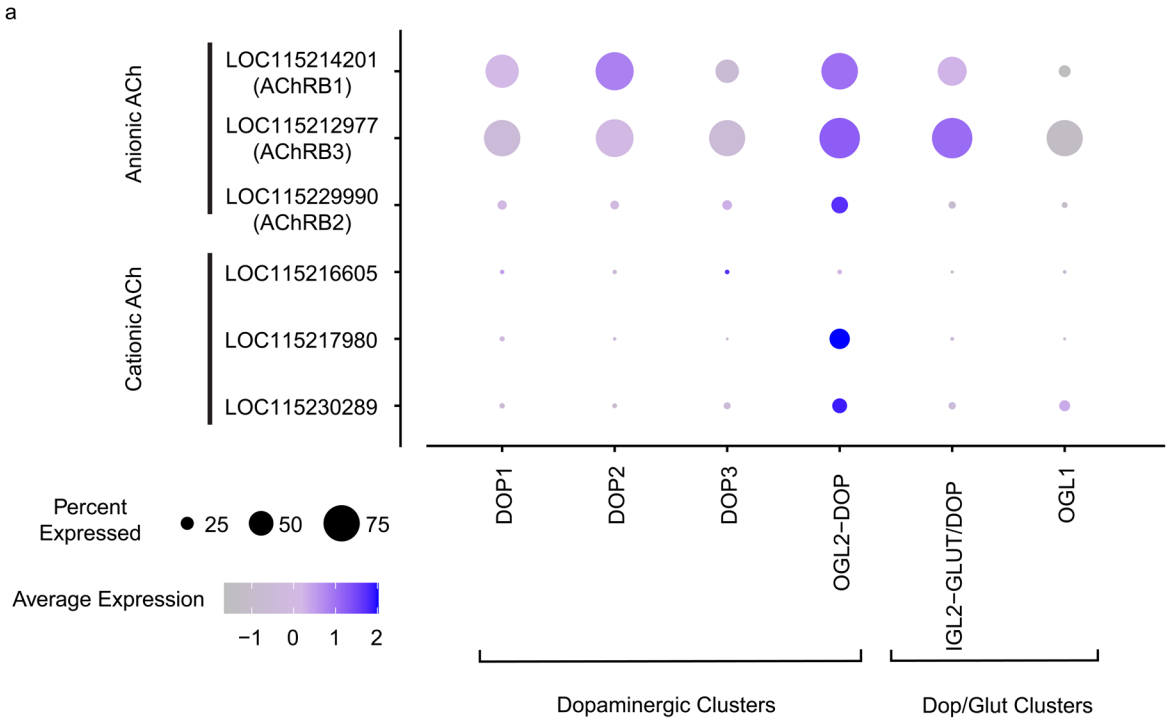

1058

1059 **Supp Fig. 14 Expression analysis of anionic and cationic ACh-gated channels in**

1060 **dopaminergic and Dop/Glut cells**

1061 Dot plot of exclusively dopaminergic and Dop/Glut clusters from the scRNA-seq of the *O. vulgaris* paralarval

1062 brain[9], showing the expression of anionic and cationic ACh genes (**A**). The size of the dots relates to the percent

1063 of cells in that cluster that express the gene, the heat map corresponds to the average expression of the gene in

1064 all cells in the cluster.

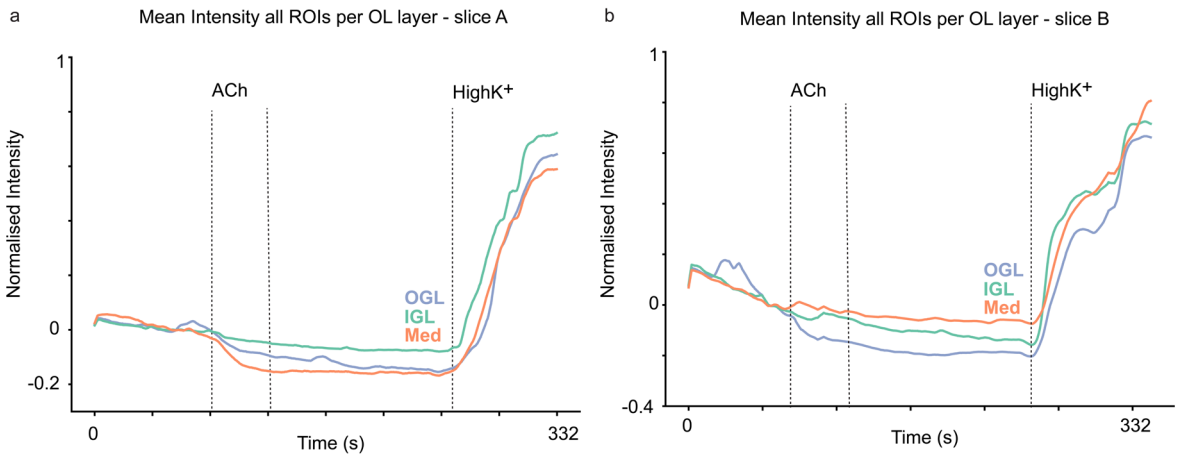

1065

1066 **Supp Fig. 15 Additional analysis of calcium imaging on acute brain slices from *O.***

1067 ***vulgaris* paralarvae during application of ACh**

1068 Calcium imaging was performed on acute brain slices from 1-dph *O. vulgaris* paralarvae during application of

1069 100 µM ACh and HighK$^+$. The mean intensity over time for all ROIs in each OL layer are plotted as purple

1070 (OGL), green (IGL) and orange (Med) lines. Two different slices have been plotted (**A** and **B**). HighK$^+$: high

1071 potassium solution, ACh: acetylcholine, OGL: outer granular layer, IGL: inner granular layer, Med: medulla.

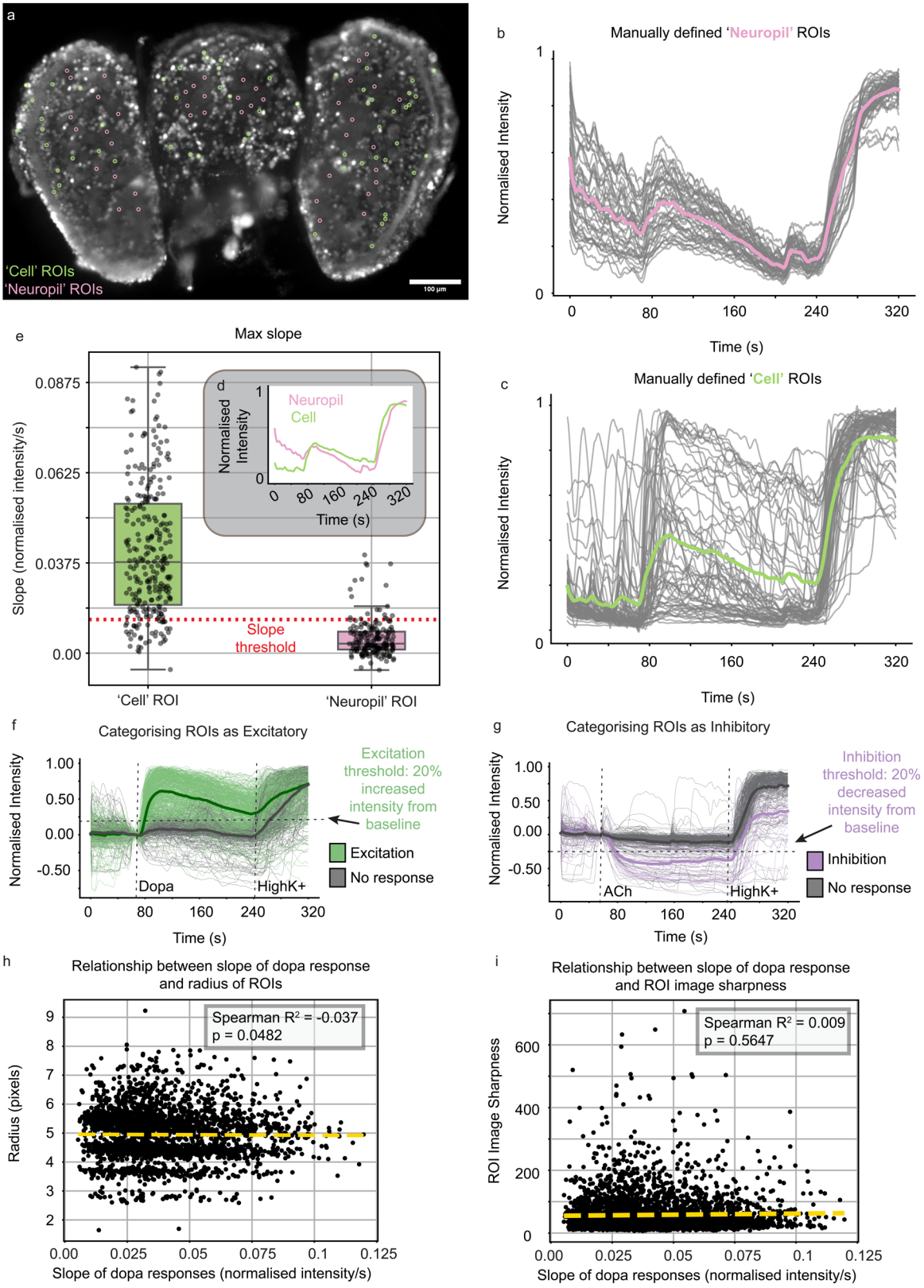
a
'Cell' ROIs
'Neuropil' ROIs
100 µm
b
Manually defined 'Neuropil' ROIs
Normalised Intensity
Time (s)
c
Manually defined 'Cell' ROIs
Normalised Intensity
Time (s)
d
Normalised Intensity
Neuropil
Cell
Time (s)
e
Max slope
Slope (normalised intensity/s)
Slope threshold
'Cell' ROI
'Neuropil' ROI
f
Categorising ROIs as Excitatory
Normalised Intensity
Excitation threshold: 20% increased intensity from baseline
Excitation
No response
Dopa
HighK+
Time (s)
g
Categorising ROIs as Inhibitory
Normalised Intensity
Inhibition threshold: 20% decreased intensity from baseline
Inhibition
No response
ACh
HighK+
Time (s)
h
Relationship between slope of dopa response and radius of ROIs
Spearman R² = -0.037
p = 0.0482
Radius (pixels)
Slope of dopa responses (normalised intensity/s)
i
Relationship between slope of dopa response and ROI image sharpness
Spearman R² = 0.009
p = 0.5647
ROI Image Sharpness
Slope of dopa responses (normalised intensity/s)

1072

1073 **Supp Fig. 16 Calcium imaging methodology**

1074 Calcium imaging was performed on acute brain slices from 1-dph *O. vulgaris* paralarvae. Maximum intensity
1075 projection of a representative brain slice used for calcium imaging with manually defined ROIs for 'Neuropil'
1076 (pink) and 'Cells' (green) (**A**). Normalised mean intensity over time for all manually defined 'Neuropil' ROIs
1077 from A in grey. Mean trace is represented in pink (**B**). Normalised mean intensity over time for all manually
1078 defined 'Cell' ROIs from A in grey. Mean trace is represented in green (**C**). Mean 'Neuropil' and 'Cell' ROIs
1079 from B and C overlayed (**D**) The max slope was calculated for all manually defined 'Cell' and 'Neuropil' ROIs
1080 from five slices from five different paralarvae used for calcium imaging (**E**). The red dotted line is the mean +
1081 standard deviation of the 'Neuropil' ROI max slope. The normalised intensity of all traces from a representative
1082 slice that was exposed to 100 µM dopamine and HighK$^+$ (**F**). The traces that were categorised as 'excitation' are
1083 in green and the traces that were categorised as 'no response' are in grey. The mean trace for each group is
1084 highlighted as a thicker grey or green trace. The normalised intensity of all traces from a representative slice that
1085 was exposed to 100 µM ACh and HighK$^+$ (**G**). The traces that were categorised as 'inhibition' are in purple and
1086 the traces that were categorised as 'no response' are in grey. The mean trace for each group is highlighted as a
1087 thicker grey or green trace. A scatter plot comparing the relationship between the radius of a cell ROI (**H**) or the
1088 sharpness of the image surrounding a ROI (**I**) and the slope of excitatory dopaminergic responses. The results of
1089 a Spearman correlation test are seen as a dotted yellow line. Scale bar: 100 µm, Dopa: dopamine, ACh:
1090 acetylcholine, HighK$^+$: high potassium solution, ROI: region of interest.

1091 # Supplemental files

1092 Supplemental file 1 – names and gene IDs for all receptors functionally characterised in this
1093 study.

1094 Supplemental file 2 – citations for all receptors included in the phylogenetic tree which had a
1095 functional annotation.

1096 Supplemental file 3 – protein sequence alignment for 'cys-loop' LGCs from major metazoan
1097 phyla.

Supplemental file 4 – full phylogenetic tree for 'cys-loop' LGCs from major metazoan phyla. All receptors that have been previously functionally characterised have their ligand highlighted in yellow.

Supplemental file 5 – list of HCR probes used in this study.

Supplemental file 6 – stl file for 3D printed cylinder used as a temporary well during calcium imaging experiments.

Bibliography

1 Young, J. Z. THE NUMBER AND SIZES OF NERVE CELLS IN OCTOPUS. *Proceedings of the Zoological Society of London* **140**, 229-254 (1963). https://doi.org:https://doi.org/10.1111/j.1469-7998.1963.tb01862.x

2 Kverková, K. *et al.* The evolution of brain neuron numbers in amniotes. *Proceedings of the National Academy of Sciences* **119**, e2121624119 (2022). https://doi.org:10.1073/pnas.2121624119

3 Hochner, B., Shomrat, T. & Fiorito, G. The octopus: a model for a comparative analysis of the evolution of learning and memory mechanisms. *The Biological bulletin* **210**, 308-317 (2006). https://doi.org:10.2307/4134567

4 Vitti, J. J. Cephalopod Cognition in an Evolutionary Context: Implications for Ethology. *Biosemiotics* **6**, 393-401 (2013). https://doi.org:10.1007/s12304-013-9175-7

5 Pungor, J. R. & Niell, C. M. The neural basis of visual processing and behavior in cephalopods. *Current Biology* **33**, R1106-R1118 (2023). https://doi.org:https://doi.org/10.1016/j.cub.2023.08.093

6 Young, J. Z. The optic lobes of Octopus vulgaris. *Philosophical transactions of the Royal Society of London. Series B, Biological sciences* **245**, 19-58 (1962).

7 Pungor, J. R., Allen, V. A., Songco-Casey, J. O. & Niell, C. M. Functional organization of visual responses in the octopus optic lobe. *Current Biology* **33**, 2784-2793.e2783 (2023). https://doi.org:10.1016/j.cub.2023.05.069

8 Demb, J. B. & Singer, J. H. Functional Circuitry of the Retina. *Annual Review of Vision Science* **1**, 263-289 (2015). https://doi.org:https://doi.org/10.1146/annurev-vision-082114-035334

9 Styfhals, R. *et al.* Cell type diversity in a developing octopus brain. *Nature communications* **13**, 7392 (2022). https://doi.org:10.1038/s41467-022-35198-1

10 Songco-Casey, J. O. *et al.* Cell types and molecular architecture of the Octopus bimaculoides visual system. *Current Biology* **32**, 5031-5044.e5034 (2022). https://doi.org:https://doi.org/10.1016/j.cub.2022.10.015

11 Gisselmann, G., Pusch, H., Hovemann, B. T. & Hatt, H. Two cDNAs coding for histamine-gated ion channels in D. melanogaster. *Nature neuroscience* **5**, 11-12 (2002). https://doi.org:10.1038/nn787

12 Ringstad, N., Abe, N. & Horvitz, H. R. Ligand-gated chloride channels are receptors for biogenic amines in C. elegans. *Science* **325**, 96-100 (2009). https://doi.org:10.1126/science.1169243

13 Morud, J. *et al.* Deorphanization of novel biogenic amine-gated ion channels identifies a new serotonin receptor for learning. *Current biology : CB* (2021). https://doi.org:10.1016/j.cub.2021.07.036

14 Hardege, I., Morud, J., Courtney, A. & Schafer, W. R. A Novel and Functionally Diverse Class of Acetylcholine-Gated Ion Channels. *The Journal of neuroscience : the official journal of the Society for Neuroscience* **43**, 1111-1124 (2023). https://doi.org:10.1523/JNEUROSCI.1516-22.2022

15 Nixon, M. & Mangold, K. The early life of Octopus vulgaris (Cephalopoda: Octopodidae) in the plankton and at settlement: a change in lifestyle. *Journal of Zoology* **239**, 301-327 (1996).

16 Giuditta, A., Libonati, M., Packard, A. & Prozzo, N. Nuclear counts in the brain lobes ofoctopus vulgaris as a function of body size. *Brain research* **25**, 55-62 (1971).

17 Elagoz, A. M., Van Dijck, M., Lassnig, M. & Seuntjens, E. Embryonic development of a centralised brain in coleoid cephalopods. *Neural development* **19**, 8 (2024). https://doi.org:10.1186/s13064-024-00186-2

18 Villanueva, R. & Norman, M. D. in *Oceanography and marine biology* 111-208 (CRC Press, 2008).

19 Lees, A. J. Dopamine agonists in Parkinson's disease: a look at apomorphine. *Fundamental & Clinical Pharmacology* **7**, 121-128 (1993). https://doi.org:https://doi.org/10.1111/j.1472-8206.1993.tb00226.x

20 van Nierop, P. *et al.* Identification of Molluscan Nicotinic Acetylcholine Receptor (nAChR) Subunits Involved in Formation of Cation- and Anion-Selective nAChRs. *The Journal of Neuroscience* **25**, 10617 (2005). https://doi.org:10.1523/JNEUROSCI.2015-05.2005

21 MacDonald, K. *et al.* Functional Characterization of a Novel Family of Acetylcholine-Gated Chloride Channels in Schistosoma mansoni. *PLOS Pathogens* **10**, e1004181 (2014). https://doi.org:10.1371/journal.ppat.1004181

22 Jensen, M. L., Schousboe, A. & Ahring, P. K. Charge selectivity of the Cys-loop family of ligand-gated ion channels. *Journal of neurochemistry* **92**, 217-225 (2005). https://doi.org:10.1111/j.1471-4159.2004.02883.x

23 Young, J. Z. *The anatomy of the nervous system of Octopus vulgaris*. (Clarendon Press, 1971).

24 Chrachri, A. & Williamson, R. Dopamine modulates synaptic activity in the optic lobes of cuttlefish, Sepia officinalis. *Neuroscience letters* **377**, 152-157 (2005). https://doi.org:https://doi.org/10.1016/j.neulet.2004.11.089

25 Green, K. A. & Cottrell, G. A. Dopamine directly activates a ligand-gated channel in snail neurones. *Pflügers Archiv* **431**, 639-644 (1996). https://doi.org:10.1007/BF02191914

26 Ranganathan, R., Cannon, S. C. & Horvitz, H. R. MOD-1 is a serotonin-gated chloride channel that modulates locomotory behaviour in C. elegans. *Nature* **408**, 470-475 (2000). https://doi.org:10.1038/35044083

27 Lam, D. M. K., Wiesel, T. N. & Kaneko, A. Neurotransmitter synthesis in cephalopod retina. *Brain research* **82**, 365-368 (1974). https://doi.org:https://doi.org/10.1016/0006-8993(74)90621-0

28 Norton, A. C., Fukada, Y., Motokawa, K. & Tasaki, K. An investigation of the lateral spread of potentials in the octopus retina. *Vision Research* **5**, 253-267 (1965). https://doi.org:https://doi.org/10.1016/0042-6989(65)90003-9

29 Gavriouchkina, D. *et al.* A single-cell atlas of bobtail squid visual and nervous system highlights molecular principles of convergent evolution. *bioRxiv*, 2022.2005.2026.490366 (2022). https://doi.org:10.1101/2022.05.26.490366

30 Piscopo, S. *et al.* Pre- and postsynaptic excitation and inhibition at octopus optic lobe photoreceptor terminals; implications for the function of the 'presynaptic bags'. *European Journal of Neuroscience* **26**, 2196-2203 (2007). https://doi.org:https://doi.org/10.1111/j.1460-9568.2007.05833.x

31 Almansa, E. *et al.* in *Aquaculture and Living Resource Management – Volume 2* (ed P.L. Pereira) (CRC Press (Taylor & Francis Group), 2025).

32 Destanović, D. *et al.* A chromosome-level reference genome for the common octopus, Octopus vulgaris (Cuvier, 1797). *G3 Genes|Genomes|Genetics* **13**, jkad220 (2023). https://doi.org:10.1093/g3journal/jkad220

33 Wijckmans, E. *et al.* Functional and Biochemical Characterization of Alvinella pompejana Cys-Loop Receptor Homologues. *PloS one* **11**, e0151183 (2016). https://doi.org:10.1371/journal.pone.0151183

1184 34 Leclère, L. *et al.* The genome of the jellyfish Clytia hemisphaerica and the evolution of the cnidarian
1185 life-cycle. *Nature Ecology & Evolution* **3**, 801-810 (2019). https://doi.org:10.1038/s41559-019-0833-2
1186 35 Durinck, S. *et al.* BioMart and Bioconductor: a powerful link between biological databases and
1187 microarray data analysis. *Bioinformatics* **21**, 3439-3440 (2005).
1188 https://doi.org:10.1093/bioinformatics/bti525
1189 36 Jaiteh, M., Taly, A. & Hénin, J. Evolution of Pentameric Ligand-Gated Ion Channels: Pro-Loop
1190 Receptors. *PloS one* **11**, e0151934 (2016). https://doi.org:10.1371/journal.pone.0151934
1191 37 Krogh, A., Larsson, B., von Heijne, G. & Sonnhammer, E. L. L. Predicting transmembrane protein
1192 topology with a hidden markov model: application to complete genomes11Edited by F. Cohen. *Journal*
1193 *of molecular biology* **305**, 567-580 (2001). https://doi.org:https://doi.org/10.1006/jmbi.2000.4315
1194 38 Katoh, K. & Standley, D. M. MAFFT Multiple Sequence Alignment Software Version 7:
1195 Improvements in Performance and Usability. *Molecular biology and evolution* **30**, 772-780 (2013).
1196 https://doi.org:10.1093/molbev/mst010
1197 39 Capella-Gutiérrez, S., Silla-Martínez, J. M. & Gabaldón, T. trimAl: a tool for automated alignment
1198 trimming in large-scale phylogenetic analyses. *Bioinformatics* **25**, 1972-1973 (2009).
1199 https://doi.org:10.1093/bioinformatics/btp348
1200 40 Minh, B. Q. *et al.* IQ-TREE 2: New Models and Efficient Methods for Phylogenetic Inference in the
1201 Genomic Era. *Molecular biology and evolution* **37**, 1530-1534 (2020).
1202 https://doi.org:10.1093/molbev/msaa015
1203 41 Bianchini, G. & Sánchez-Baracaldo, P. TreeViewer: Flexible, modular software to visualise and
1204 manipulate phylogenetic trees. *Ecology and Evolution* **14**, e10873 (2024).
1205 https://doi.org:https://doi.org/10.1002/ece3.10873
1206 42 Liman, E. R., Tytgat, J. & Hess, P. Subunit stoichiometry of a mammalian K+ channel determined by
1207 construction of multimeric cDNAs. *Neuron* **9**, 861-871 (1992).
1208 https://doi.org:https://doi.org/10.1016/0896-6273(92)90239-A
1209 43 Hao, Y. *et al.* Integrated analysis of multimodal single-cell data. *Cell* **184**, 3573-3587.e3529 (2021).
1210 https://doi.org:10.1016/j.cell.2021.04.048
1211 44 Deryckere, A., Styfhals, R., Elagoz, A. M., Maes, G. E. & Seuntjens, E. Identification of neural
1212 progenitor cells and their progeny reveals long distance migration in the developing octopus brain.
1213 *eLife* **10**, e69161 (2021). https://doi.org:10.7554/eLife.69161

1214 45 Kuehn, E. *et al.* Segment number threshold determines juvenile onset of germline cluster expansion in
1215 Platynereis dumerilii. *Journal of Experimental Zoology Part B: Molecular and Developmental*
1216 *Evolution* **338**, 225-240 (2022). https://doi.org:https://doi.org/10.1002/jez.b.23100
1217 46 Elagoz, A. M. *et al.* Optimization of Whole Mount RNA Multiplexed in situ Hybridization Chain
1218 Reaction With Immunohistochemistry, Clearing and Imaging to Visualize Octopus Embryonic
1219 Neurogenesis. *Frontiers in Physiology* **13** (2022). https://doi.org:10.3389/fphys.2022.882413
1220 47 Schindelin, J. *et al.* Fiji: an open-source platform for biological-image analysis. *Nature methods* **9**, 676-
1221 682 (2012). https://doi.org:10.1038/nmeth.2019
1222 48 Stringer, C. & Pachitariu, M. Cellpose3: one-click image restoration for improved cellular
1223 segmentation. *Nature methods* **22**, 592-599 (2025). https://doi.org:10.1038/s41592-025-02595-5
1224 49 Pachitariu, M. *et al.* Suite2p: beyond 10,000 neurons with standard two-photon microscopy. *bioRxiv*,
1225 061507 (2017). https://doi.org:10.1101/061507
1226 50 Bansal, R., Raj, G. & Choudhury, T. in *2016 International Conference System Modeling &*
1227 *Advancement in Research Trends (SMART).* 63-67.
1228 51 Deryckere, A., Styfhals, R., Elagoz, A. M., Maes, G. E. & Seuntjens, E. Identification of neural
1229 progenitor cells and their progeny reveals long distance migration in the developing octopus brain.
1230 *Elife* **10** (2021). https://doi.org:10.7554/eLife.69161

1231 Acknowledgements

1232 The authors gratefully acknowledge Denise Walker and all other past and present members of
1233 the Schafer and Seuntjens labs for technical assistance and helpful discussions. *Dapnia*
1234 *magna* were kindly provided by the labs of Robby Stoks and Luc De Meester from KU
1235 Leuven, Belgium. The authors thank Joshua Rosenthal from the Marine Biological
1236 Laboratory for kindly providing the *Octopus bimaculoides* AChRB1 *Xenopus* plasmid. The
1237 authors also wish to acknowledge Gáspár Jékely and Milena Marinković from the Living
1238 Systems Institute, University of Exeter, for their advice on the phylogenetic analysis. The
1239 authors also wish to thank the Arckens lab for kindly allowing us to use their equipment for
1240 the calcium imaging experiments. Jon Howe and the LMB microscopy facilities team offered

state of the art imaging facilities and expertise which the authors were very grateful for. The authors are also grateful to Benjamin Jenkins from the University of Cambridge for his expert advice on phylogenetic analysis. We would also like to thank the LMB Scientific Computing team and Rory Bedford for assistance with using the computer clusters. The authors are also grateful to all members of the VisLab team, particularly Elfy Chiang. Finally, the authors wish to thank all support and administrative staff at the LMB and KU Leuven.

Author Contributions

A.C., E.S., and W.R.S conceptualised the project and designed the experiments. A.C. carried out the phylogenetic analysis. E.A. supplied the *O. vulgaris* paralarvae. A.C., I.H., and J.G.R. performed the *Xenopus* oocyte electrophysiology experiments. R.S. and M.Las. prepared *O. vulgaris* and *D. magna* cDNA. A.C., R.S., L.G., M.Lan., and A.M.J. performed the HCR experiments and acquired the images. J.B. developed the HCR image analysis pipeline and A.C. carried out the analysis and visualisation. A.C., R.S., and M.V.D. optimised and carried out the calcium imaging experiments. A.C. and H.A.O. developed the calcium image analysis pipeline and A.C. carried out the analysis and visualisation. A.C., E.S., and W.R.S wrote the original manuscript, and all authors read and critically revised the manuscript. E.S. and W.R.S supervised the project and provided funding/infrastructure.

Funding

This work was kindly supported by the Medical Research Council MC-A023-5PB91 (to W.R.S.), the Research Foundation – Flanders G079521N (to W.R.S.), G040124N (to E.S.) and fellowships 11L1923N (to M.Las) and 1181025N (to M.V.D.), and KU Leuven BOF C14/16/049 (to E.S. and W.R.S.) and ID-N/20/007 (to E.S.).

Declaration of Interests

The authors declare no competing interests.